PHYSICAL REVIEW B **103**, 155301 (2021)

Superradiantlike dynamics of nuclear spins by nonadiabatic electron shuttling

Yinan Fang,[1,2,3,9] Ying-Dan Wang,[4,5,6,2] Rosario Fazio,[2,7,1] and Stefano Chesi[1,8,*]
[1] *Beijing Computational Science Research Center, Beijing 100193, China*
[2] *ICTP, Strada Costiera 11, I-34151 Trieste, Italy*
[3] *Department of Physics, McGill University, 3600 Rue University, Montreal, Quebec, Canada H3A 2T8*
[4] *CAS Key Laboratory of Theoretical Physics, Institute of Theoretical Physics, Chinese Academy of Sciences, Beijing 100190, China*
[5] *School of Physical Sciences & CAS Center for Excellence in Topological Quantum Computation, University of Chinese Academy of Sciences, Beijing 100049, China*
[6] *Synergetic Innovation Center for Quantum Effects and Applications, Hunan Normal University, Changsha 410081, China*
[7] *Dipartimento di Fisica, Universita' di Napoli "Federico II", Monte S. Angelo, I-80126 Napoli, Italy*
[8] *Department of Physics, Beijing Normal University, Beijing 100875, China*
[9] *Department of Physics, Yunnan University, Kunming 650091, China*

(Received 5 February 2020; revised 5 March 2021; accepted 8 March 2021; published 1 April 2021)

We investigate superradiantlike dynamics of a nuclear-spin bath in contact with an electron shuttle, modeled as a moving quantum dot trapping a single electron. The dot is shuttled between two external reservoirs, where electron-nuclear flip flops are associated with tunneling events. For an ideal model with uniform hyperfine interaction, realized through an isotopically enriched "nuclear-spin island", we discuss in detail the nuclear spin evolution and its relation to superradiance. We then show that the superradiantlike evolution is robust to various extensions of the initial setup, and derive the minimum shuttling time which allows to escape adiabatic spin evolution. We also discuss slow/fast shuttling under the inhomogeneous field of a nearby micromagnet and compare our scheme to a model with stationary quantum dot. Finally, we describe the electrical detection of nuclear entanglement in the framework of Monte Carlo wave-function simulations.

DOI: 10.1103/PhysRevB.103.155301

I. INTRODUCTION

Coherent control of spins in solid-state systems is a subject of intense research, both from the point view of fundamental physics and future applications. In quantum dots, efforts to prolong the coherence time of electronic spins has led to a greatly improved understanding of the coupling with the nuclear-spin bath [1–3]. Although isotropically purified devices represent an attractive option, the nuclear-spin bath leads to interesting physical effects and might be turned into a useful quantum resource. Potential applications include the realization of quantum memories [4] and small quantum registers [5], similar to what has been already demonstrated with single donors and defects [6–8].

In current quantum dots devices, the effect of nuclear spins can be often understood well through their polarization. For example, it is possible to monitor in time the evolution of the Overhauser field and characterize its noise spectrum [9–11]. Modeling the effect of nuclear spins as a stochastic classical field has also been very useful in describing decoherence at short time scales [12,13], and to develop efficient dynamical decoupling techniques [14,15]. Furthermore, dynamical nuclear polarization (DNP) allows to influence actively the nuclear-spin polarization, by achieving relatively large values and/or narrowing its distribution [2,14,16–18,53–57]. Despite these successes, however, this physics is insensitive to intrinsic quantum features of the nuclear-spin state.

An interesting possibility to go beyond these effects, and generate entanglement in the nuclear spin-bath in a controlled and easily detectable way, is based on inducing a superradiantlike evolution [19–22]. These proposals are guided by an analogy between the hyperfine Hamiltonian and the Dicke model of optical superradiance [20,23–26], with the nuclear spins playing the role of two-level atoms and the tunneling of electrons analogous to photon emission. The setup is usually in a spin-blocked configuration, where election tunneling is only possible through flip-flop events allowed by the hyperfine interaction. The electron-nuclear flip flops act collectively on N nuclear spins, modifying the spin polarization and at the same time building up entanglement. Despite the similarity with DNP, a crucial feature here is the detection of entanglement, which is responsible of a large enhancement of electron tunneling rates. The maximum enhancement factor occurs for the nearly depolarized state and is of order N, with typical quantum dots having up to $N \sim 10^5$–10^6. Thus detecting the nuclear-spin entanglement should become relatively straightforward by transport or charge-sensing measurements.

In this work, we investigate the possibility of realizing the superradiantlike dynamcis in a movable quantum dot configuration, where the electron is shuttled between two external reservoirs [27–31]. As we will see, our shuttling device offers certain advantages. It does not rely on ferromagnetic contacts [22] and allows to escape the blockade regime much more

---

[*] stefano.chesi@csrc.ac.cn

©2021 American Physical Society

efficiently than other stationary configurations [20]. The mode of operation of the shuttle is rather standard for quantum dot devices, as it can be seen as a fast switching between the (1,0) and (0,1) configurations of a double quantum dot.

More generally, our study explores an interesting interplay of spin dynamics and shuttling, which might be relevant for a variety of devices. Electron shuttles can also be realized in nanoelectro-mechanical systems with vibrating organic molecules [32], metallic grains [27], or silicon nanopillars [33] and are characterized by rich transport regimes due to the interplay of charge and mechanical degree of freedoms [34–36]. They also attract interest in the study of noise and full counting statistics [37,38]. Finally, recent progress on shuttling electrons across extended arrays of quantum dots [39,40] provides further motivations to our study.

Our article is organized as follows. In Sec. II, we present the electron shuttle model in an idealized setup. In Sec. III, we give the master equations governing the electron-nuclear spin dynamics, under the assumption of fast shuttling. In Sec. IV, we present the main results for the ideal model, which allows us to establish a precise connection with optical superradiance. In Sec. V, we relax several assumptions, showing that the superradiantlike evolution is quite robust to imperfections. In Sec. VI, we derive the important nonadiabaticity condition for the spin evolution (depending on shuttling speed). A strictly related discussion of shuttling in the slanting field of a micromagnet is also provided. In Sec. VII, we discuss the crucial role played by the nonadiabatic shuttling in weak-tunneling setups. Finally, in Sec. VIII, we present an alternative analysis in terms of Monte Carlo wave-function simulations. Further technical details can be found in Appendices A and B.

II. MODEL

We start by considering an ideal setup of the shuttle, schematically illustrated in Fig. 1. We model it as a moving quantum dot, whose time-dependent position $x(t)$ (i.e., the minimum of the confining potential) can be controlled externally. A shuttling motion is imposed between left and right operating points, which are in contact with external leads. To simplify matters, we initially suppose that a nuclear-spin rich region is only embedded at the right position ($x = L/2$) while at the left position ($x = -L/2$, poor in nuclear spins) the hyperfine interaction is effectively turned off.

Introducing a spatially localized "nuclear-spin island" is motivated by a recent proposal for approaching nearly uniform hyperfine interactions [22]. This condition leads to a simple integrable Hamiltonian, which is in direct analogy to the Dicke model. Furthermore, when nuclear spins are only included at one of the two operation points, shuttling allows to separate spatially the electron-spin initialization (left position) from the entangled electron-nuclear dynamics (right position). In Sec. V, we will see how these assumptions facilitate the superradiantlike dynamics, but are not strictly necessary.

A. Hyperfine interaction and tunnel couplings

To specify the Hamiltonian, it is convenient to consider first a given value of x, which fixes the hyperfine and

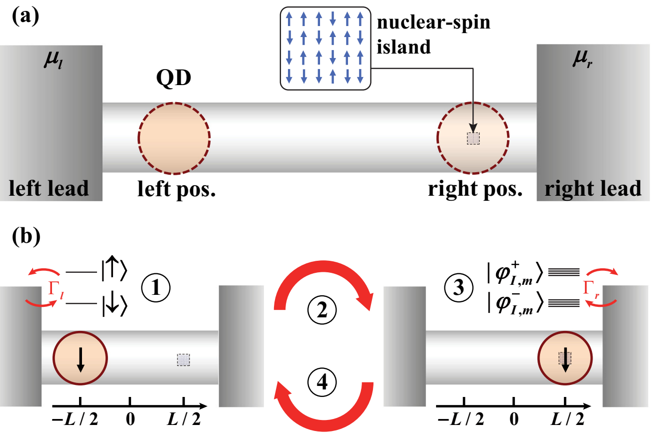

FIG. 1. (a) Schematics of the electron shuttle. An excess electron resides on the orbital ground state of the instantaneous trapping potential, forming a moving quantum dot (QD). The trapping potential can be controlled between a nuclear-spin free region (left position, at $x = -L/2$) and a nuclear-spin rich region (right position, at $x = L/2$) [22]. The size of the QD envelope function is significantly larger than the nuclear region, allowing a "box-model" description for their coherent coupling [41–43]. (b) Shuttling cycle. In step 1 (step 3), the dot is tunnel-coupled to the left (right) external lead, with energy levels as schematically illustrated. Steps 2 and 4 are fast shuttling processes between $x = \pm L/2$.

tunnel couplings at their instantaneous values. We suppose that the shuttling is sufficiently slow, such that during the whole process the electrons occupy the instantaneous orbital ground state of the quantum dot. Furthermore, due to a large Coulomb repulsion, we neglect doubly-occupied states. At a given value of x, the singly-occupied states are $d_\sigma^\dagger|0\rangle$, where $|0\rangle$ is the state with no electrons in the dot, $d_\sigma^\dagger$ is a fermionic creation operator, and $\sigma = \uparrow, \downarrow$ is the spin index. The full Hamiltonian reads

$$H = H_0 + H_T + H_b, \tag{1}$$

where the isolated dot is described by ($\hbar = 1$):

$$H_0 = \sum_\sigma \epsilon_\sigma d_\sigma^\dagger d_\sigma + \frac{A}{N_d}\mathbf{S}\cdot\mathbf{I}, \tag{2}$$

where $\omega_0 = \epsilon_\uparrow - \epsilon_\downarrow = g\mu_B B_z$ is the Zeeman splitting due to an external magnetic field in the z direction and the second term is the hyperfine interaction, with $S^\alpha = \frac{1}{2}\sum_{ss'}\sigma^\alpha_{ss'}d_s^\dagger d_{s'}$ ($\boldsymbol{\sigma}$ is the vector of Pauli matrices) the electron spin operators and $I^\alpha = \sum_{i=1}^N I_i^\alpha$ the collective spin operators of N nuclear spins.

In general, the coupling strength of the hyperfine interaction for a nuclear spin at position $\mathbf{r}_k$ has the form $Av_0|\psi(\mathbf{r}_k)|^2$, where the energy scale A depends on the nuclear isotope and the electronic states of the host crystal, v_0 is the atomic volume, and $\psi(\mathbf{r})$ is the envelope function of the quantum dot [1,42,44]. Here we have approximated $Av_0|\psi(\mathbf{r}_k)|^2 \simeq A/N_d$, which is justified under special circumstances. For example, Ref. [22] proposed to realize approximately uniform hyperfine couplings through a nuclear-spin island. As discussed there, the concept might be implemented in a Si/Ge core-shell nanowire with a segment of its inner core being isotopically modulated to host a ^{29}Si section of nanometer size [45,46]. Alternatively, the right position $x = L/2$ could host one or few magnetic impurities [47]. We note that N_d is of the order of the number of lattice sites having significant overlap with the quantum dot. Thus, for materials with spinless isotopes, N can be significantly smaller than N_d.

Taking into account the nuclear spins, the empty quantum dot is simply described by $|0, m\rangle \equiv |0\rangle \otimes |I, m\rangle$, where $|I, m\rangle$ are the eigenstates of I^2, I^z with eigenvalues $I(I+1)$ and m, respectively (we omit permutational quantum numbers). In the basis $|\sigma, m\rangle \equiv d_\sigma^\dagger|0\rangle \otimes |I, m\rangle$, the eigenstates with one electron are given by

$$\begin{aligned} |\varphi^-_{I,m}\rangle &= \alpha_{m-1}|\downarrow, m\rangle - \beta_{m-1}|\uparrow, m-1\rangle, \\ |\varphi^+_{I,m}\rangle &= \alpha_m|\uparrow, m\rangle + \beta_m|\downarrow, m+1\rangle, \end{aligned} \tag{3}$$

where $m \in [-I, I]$ and, conventionally, $|\uparrow, -I-1\rangle = |\downarrow, I+1\rangle = 0$. The amplitudes are $\alpha_m = \cos(\theta_m/2)$ and $\beta_m = \sin(\theta_m/2)$, with the mixing angle:

$$\theta_m = \arg\left[\frac{1}{2\eta} + m + \frac{1}{2} + i\sqrt{I(I+1) - m(m+1)}\right]. \tag{4}$$

The parameter η is the ratio of hyperfine coupling and Zeeman energy:

$$\eta = \frac{A/N_d}{2\omega_0}, \tag{5}$$

and will play an important role in the rest of the paper. For typical quantum dots, $\eta \ll 1$ under a moderate magnetic field and we will also restrict ourselves to this condition. For example, using values appropriate to Si quantum dots [48] $A \simeq 2\ \mu$eV, $\omega_0 = 10\ \mu$eV (i.e., $B_z \simeq 0.1$ T), and $N_d = 10^5$, one obtains $\eta \simeq 10^{-6}$. Finally, the energies of $|\varphi^\pm_{I,m}\rangle$ are

$$\epsilon^\pm_{I,m} = \bar{\epsilon} \pm \frac{\omega_0}{2}\sqrt{1 + \eta(4m \pm 2) + \eta^2(2I+1)^2} - \frac{\eta\omega_0}{2}, \tag{6}$$

where we defined $\bar{\epsilon} = (\epsilon_\uparrow + \epsilon_\downarrow)/2$. Usually (except around $\eta I = 1/2$), the $\pm$ sets of levels form two well-separated energy bands. In particular, when $\eta I \ll 1$ the gap is close to ω_0. We choose the level alignment as in Fig. 1(b), where $\epsilon^+_{I,m} > \mu_{l,r} > \epsilon^-_{I,m}$.

The quantum dot is connected to two external leads through a standard tunnel Hamiltonian:

$$H_T = \sum_{\alpha,k,\sigma} T_{\alpha k} d_\sigma^\dagger c_{\alpha k\sigma} + \text{H.c.}, \tag{7}$$

with spin-independent tunnel amplitudes, $T_{\alpha k}$ and $\alpha = l, r$ labeling the left and right lead, respectively. H_b is

$$H_b = \sum_{\alpha,k,\sigma} \varepsilon_{\alpha k} c^\dagger_{\alpha k\sigma} c_{\alpha k\sigma}, \tag{8}$$

where we assume that the reservoirs are unpolarized, thus the single-particle energies $\varepsilon_{\alpha k}$ are spin-independent. As a consequence, the density of states $n_\alpha(\varepsilon)$ are spin-independent as well. The occupation numbers are given by $f_\alpha(\varepsilon) = \{\exp[\beta(\varepsilon - \mu_\alpha)] + 1\}^{-1}$ where we generally assume the low-temperature regime:

$$f_\alpha(\varepsilon) \simeq \theta(\mu_\alpha - \varepsilon). \tag{9}$$

Although other choices are possible, the desired spin dynamics can be generated without an applied bias. Therefore we will assume $\mu_l = \mu_r$, as illustrated in Fig. 1(b).

B. Electron shuttle

While in some shuttling setups it is necessary to solve a separate dynamical equation for the moving center $x(t)$, depending on the evolution of the internal variables of the shuttle (e.g., its charge state [27]), here we assume that the motion is determined by external controls. In particular, we neglect the small back-action on the electron motion from its internal spin dynamics. The main consequence of the $x(t)$ parametric dependence is to induce time-dependent tunnel and hyperfine couplings in the system Hamiltonian, Eq. (1).

As represented in Fig. 1, the right and left operating points are at $x_l = -L/2$ and $x_r = L/2$, respectively. When the electron shuttle moves close to x_l (x_r) it interacts more strongly with the left (right) lead. We can write explicitly the x-dependence of the tunnel amplitudes in Eq. (7) as follows:

$$T_{\alpha k}(x) \simeq T_\alpha e^{-|x-x_\alpha|/\lambda_\alpha}, \tag{10}$$

where $\lambda_{l,r}$ are the tunneling lengths [27,36,49]. Here we have also made the usual approximations that $T_{\alpha k}$ is independent of k. For simplicity, we will consider $\lambda_{l,r} \ll L$, such that an electron at x_l (x_r) can only interact with the left (right) reservoir. Further assuming $n_\alpha(\varepsilon) \simeq n_\alpha$, the tunneling rates at the left/right positions are

$$\Gamma_\alpha = 2\pi n_\alpha |T_\alpha|^2, \tag{11}$$

which we choose to be in the weak-tunneling regime, $\Gamma_\alpha \ll |\mu_\alpha - \epsilon^\pm_{I,m}|$.

Similarly, the spatial dependence of the hyperfine interaction could be of the type:

$$A(x) = Ae^{-(L/2-x)^2/\Delta x^2}, \tag{12}$$

where we take into account a Gaussian envelope wave function (appropriate for a harmonic confinement centered in x). To have all the hyperfine couplings approximately equal, the spatial extent of the nuclear-spin rich region should be smaller than Δx. Furthermore, we will typically assume $\Delta x \ll L$ such that the hyperfine coupling is only significant when $x \simeq L/2$. The assumption of uniform coupling is more accurate when the center of the electron's wave function sits on top of the small nuclear-spin island [22]. At this position, the hyperfine coupling is largest.

III. DYNAMICAL EVOLUTION

We would like to model the electron-nuclear spin dynamics under a cyclic operation, where the electron continuously shuttles between the left and right positions of Fig. 1. There is considerable freedom in designing such cycle. However, we will first assume that the two shuttling processes between $x = \pm L/2$ are sufficiently fast to treat them as instantaneous quenches (in the spin degrees of freedom). This is not in contrast with the adiabatic assumption about the orbital ground state, as typical orbital energies are much larger than the Zeeman splitting. A detailed discussion of shuttling with finite speed is given in Sec. VI.

In summary, the mode of operation is a four-step cycle illustrated in Fig. 1(b) and comprised by: (i) initialization period t_l at $x = -L/2$, loading a single electron in the $\downarrow$ state; (ii) a fast shuttling process to the right operation point; (iii) a waiting period t_r at $x = L/2$, when the electron interacts with the nuclear spins allowing for flip-flop processes to occur; (iv) fast shuttling back to $x = -L/2$. Effectively, we treat the cycle as a two-step process with only (i) and (iii) and the period is $T \simeq t_l + t_r$.

A. Master equations

By tracing out the degrees of freedom of the two leads, the system can be described by Markovian master equations. In the first part of each cycle, we compute the evolution using:

$$\dot{\rho}_s = -i[H_z, \rho_s] + \Gamma_l(\mathcal{D}[d_\uparrow] + \mathcal{D}[d_\downarrow^\dagger])\rho_s, \tag{13}$$

where H_z is the Zeeman Hamiltonian, defined by taking $A = 0$ in Eq. (2), and the dissipator is of the Lindblad type, $\mathcal{D}[L]\rho_s = L\rho_s L^\dagger - \frac{1}{2}\{L^\dagger L, \rho_s\}$. Equation (13) is a standard master equation for a quantum dot in contact with an external reservoir (the left lead) where the chemical potential μ_l lies between the two Zeeman levels. ρ_s is the full density matrix of the system, i.e., includes both the electronic and nuclear degrees of freedom, but the nuclear dynamics is trivial in this case.

For the second part of each cycle (e.g., $t_l < t < T$), the quantum dot center lies on the top of the nuclear-spin island and it is important to take into account the hyperfine interaction. As described in Appendix A, we perform a standard derivation by tracing out the lead degrees of freedom in the second-order Born-Markov approximation. After a rotating-wave approximation (RWA), we obtain

$$\dot{\rho}_s = -i[H_0, \rho_s] + \Gamma_r \sum_\sigma (\mathcal{D}[A_{\sigma+}] + \mathcal{D}[A_{\sigma-}^\dagger])\rho_s, \tag{14}$$

where we defined the Lindblad operators:

$$A_{\sigma\pm} = d_\sigma P_\pm, \tag{15}$$

with $P_\pm = \sum_{I,m} |\varphi_{I,m}^\pm\rangle\langle\varphi_{I,m}^\pm|$ the projectors on the one-electron eigenspaces, see Eq. (3). For large Zeeman splitting (compared to the strength of hyperfine interaction), one has $A_{\uparrow+} \simeq d_\uparrow$ and $A_{\downarrow-} \simeq d_\downarrow$ while $A_{\uparrow-}, A_{\downarrow+} \simeq 0$. However, in general it is important to take into account consistently the hyperfine interaction both in the Hamiltonian and dissipative terms. As we will discuss in more detail in Sec. VII, even a small difference between d_σ and $A_{\sigma\pm}$ can have important effects on the long-time evolution.

An example of the numerical results obtained in this manner is shown in Fig. 2, where the detailed evolution of the nuclear-spin polarization $M_z(t) \equiv \mathrm{Tr}\{I^z\rho_s(t)\}$ is plotted. The result is that the periodic shuttling leads to a systematic lowering of the nuclear-spin polarization with each half-cycle. The physical mechanism behind this effect is directly related to the form of the eigenstates Eq. (3), which are superpositions of $|\downarrow, m\rangle$ and $|\uparrow, m-1\rangle$, i.e., they take into account the exchange of angular momentum between electron and nuclear spins induced by the hyperfine interaction. Since $|\varphi_{I,m}^\pm\rangle$ differ from the Zeeman eigenstates, a fast shuttling processes leads to a small probability of populating the high-energy eigenstate and allows the electron to tunnel out of the dot. Such processes are effectively associated with a flip-flop of electron and nuclear spins, thereby lowering M_z.

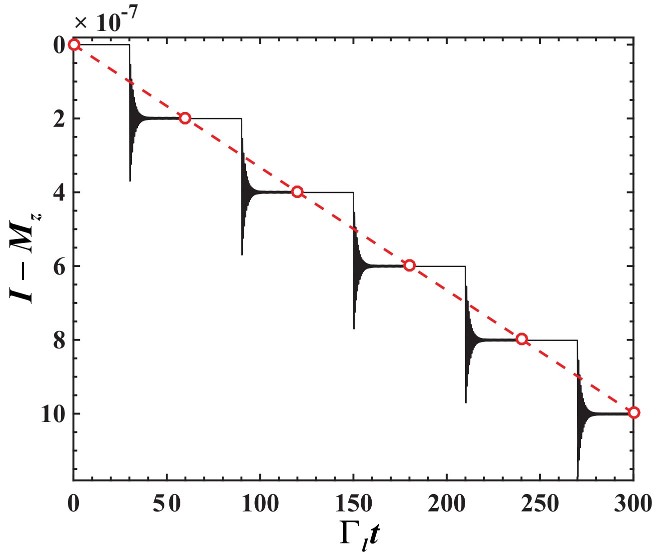

FIG. 2. Full dynamics of the cyclic shuttling process, described by instantaneous quenches between a right and left waiting periods, see Eqs. (13) and (14). Starting from $|\downarrow, N/2\rangle$ (i.e., fully polarized nuclei), we plot the full time-dependence of the nuclear-spin polarization (solid black curve) as well as its approximate stroboscopic evolution (red dashed line). Parameters (setting $\omega_0 = 1$): $N = 10$, $I = N/2$, $\eta = 1 \times 10^{-4}$, $\Gamma_l = \Gamma_r = 0.1$, $\mu_l = \mu_r = \bar{\epsilon} = 0$, and $t_l = t_r = 30\,\Gamma_{l,r}^{-1}$.

The full time evolution eventually leads to a full reversal of the nuclear-spin polarization. However, the drop of M_z at each cycle is small due to the small amplitude of flip-flop states in Eq. (3): $\beta_m \propto \eta$ gives a change in magnetization $\Delta M_z \propto \eta^2$ [see also the discussion in Sec. VII, and especially Eq. (43)]. Therefore the superradiantlike enhancement appears after many cycles, which are numerically cumbersome to simulate. In the next section we develop an approximate stroboscopic treatment which is accurate (see dashed line in Fig. 2) and is able to describe the dynamics in a more efficient and physically transparent manner.

B. Stroboscopic description

If, as in Fig. 2, the waiting times $t_{r,l}$ are relatively long compared to $\Gamma_{l,r}^{-1}$, the system approaches a (temporary) stationary state before each quench. Under these conditions, it is possible to derive a simpler stroboscopic description of the long-time evolution. More specifically, the system after n periods is described by

$$\rho_s(nT) \simeq |\downarrow\rangle\langle\downarrow| \otimes \sum_m p_m(n)|I, m\rangle\langle I, m|, \tag{16}$$

and the nuclear-spin bath populations are determined by the discrete time evolution:

$$\mathbf{p}(n) = \mathbf{A}^n \mathbf{p}(0), \tag{17}$$

where $\mathbf{p}(n) = (p_{-I}(n), p_{-I+1}(n), \ldots p_I(n))^T$ and the evolution matrix $\mathbf{A}$ is derived below.

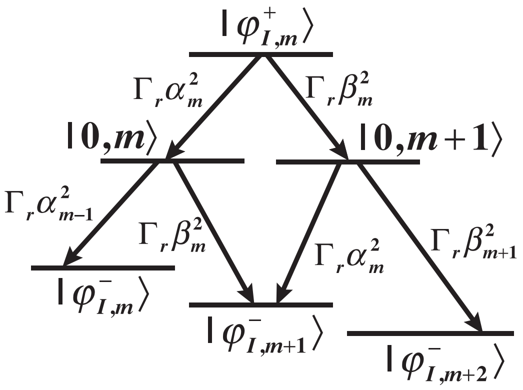

FIG. 3. Branching processes for the state $|\varphi^+_{I,m}\rangle$. The rate of each process is indicated explicitly. The rate equations can be easily obtained from Eq. (14) and are explicitly given in Eq. (B1), setting $\Gamma_l = 0$.

To obtain **A**, we first consider the electron prepared at the left position in the state $|\downarrow\rangle \otimes |I, m+1\rangle$. After the sudden quench to the right position, it is appropriate to use the eigenstates of Eq. (3), giving

$$|\downarrow, m+1\rangle = \alpha_m|\varphi^-_{I,m+1}\rangle + \beta_m|\varphi^+_{I,m}\rangle. \tag{18}$$

This state constitutes the initial condition for Eq. (14) where, due to the RWA approximation, the coherence between $|\varphi^-_{I,m+1}\rangle$ and $|\varphi^+_{I,m}\rangle$ decays to zero without affecting the population dynamics. Thus the stationary state is determined by rate equations alone.

While $|\varphi^-_{I,m+1}\rangle$ is already stationary, the high-energy state $|\varphi^+_{I,m}\rangle$ leads to the electron tunneling out of the quantum dot, followed by a process where the dot is re-occupied. The detailed branching processes for $|\varphi^+_{I,m}\rangle$, with the corresponding rates, are illustrated in Fig. 3. Taking them into account, it is seen that $|\downarrow, m+1\rangle$ evolves into a mixture of $|\varphi^-_{I,m}\rangle$, $|\varphi^-_{I,m+2}\rangle$, and $|\varphi^-_{I,m+1}\rangle$ and the final populations can be obtained as follows:

$$R_{m,m+1} = \frac{\beta_m^2\alpha_m^2\alpha_{m-1}^2}{\alpha_{m-1}^2+\beta_m^2}, \quad R_{m+2,m+1} = \frac{\beta_m^4\beta_{m+1}^2}{\alpha_m^2+\beta_{m+1}^2},$$
$$R_{m+1,m+1} = 1 - R_{m,m+1} - R_{m+2,m+1}. \tag{19}$$

If we consider the reverse shuttling process, where the electron is prepared in a $|\varphi^-_{I,m}\rangle$ eigenstate and is quickly shuttled to the (left) nuclear-spin free region, the following sequence of tunneling events becomes possible for the component of $|\varphi^-_{I,m}\rangle$ in the excited state: $|\uparrow, m-1\rangle \rightarrow |0, m-1\rangle \rightarrow |\downarrow, m-1\rangle$. It is quite clear that the final state will be a mixture of $|\downarrow, m\rangle$ and $|\downarrow, m-1\rangle$, and the populations are given by

$$L_{m,m} = \alpha_{m-1}^2, \quad L_{m-1,m} = \beta_{m-1}^2. \tag{20}$$

In summary, the effect of a full cycle at the left operating point is to induce transitions from an initial condition $|\downarrow, m+1\rangle$ to four final states, $|\downarrow, m-1\rangle, \ldots, |\downarrow, m+2\rangle$, and the transition matrix **A** entering Eq. (17) is

$$\mathbf{A} = \mathbf{L}\,\mathbf{R}, \tag{21}$$

where the nonzero matrix elements of **L**, **R** are given by Eqs. (19) and (20), after a straightforward redefinition of the indexes (from $[-I, I]$ to $[1, 2I+1]$).

As discussed in Fig. 2, we have checked that the stroboscopic description agrees well with the full time dependence. By using this approach, the long-time dynamics can be efficiently computed as in Fig. 4, where features typical of the superradiantlike evolution become apparent.

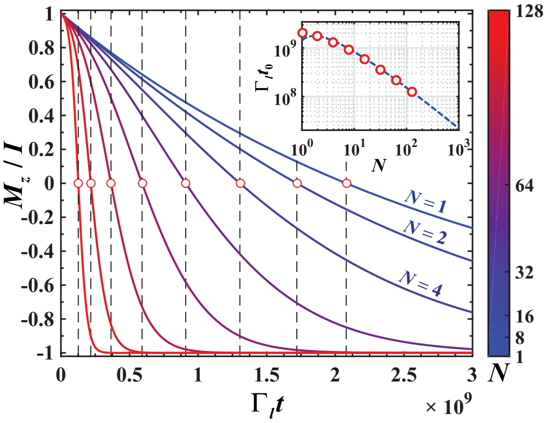

FIG. 4. Time dependence of the nuclear-spin polarization M_z at different values of $N = 1, 2, 4, \ldots, 128$ (see color code). The vertical dashed lines with red dots mark the times t_0 at which $M_z = 0$. Inset: scaling of t_0 with respect to N, where the blue dashed curve shows the theoretical prediction Eq. (24). Except N, other parameters are the same of Fig. 2, and $I = N/2$ were assumed for all curves.

IV. SUPERRADIANT-LIKE SHUTTLING

We show in Fig. 4 the long-time evolution of the nuclear-spin polarization $M_z(t)$ at increasing values of $N = 1, 2, 4, \ldots, 128$ and illustrate in Fig. 5 the evolution of the full distribution function, p_m, in the case $N = 128$. The behaviors of M_z and p_m are in good agreement with the features of optical superradiance: We see that the evolution time is reduced at larger values of N, and p_m becomes a broad

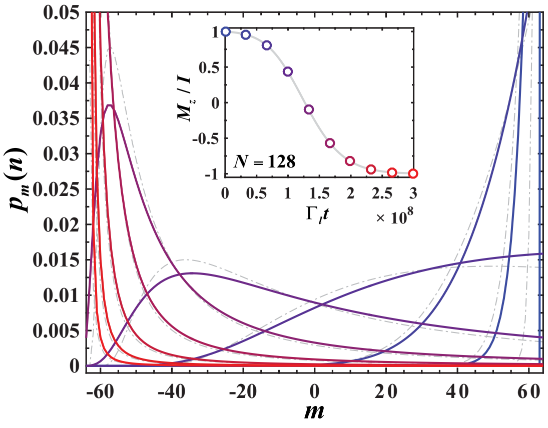

FIG. 5. Time evolution of the distribution p_m (solid lines), for the $N = 128$ ($I = N/2$) case of Fig. 4. The time of each distribution is marked in the inset with a circle of the same color. The gray dash-dotted curves show the superradiant approximation, Eq. (25).

distribution with significant weight over all values of m. The large variance at intermediate times reflects the large shot-to-shot fluctuation typical of superradiance [25,50]. In fact, through the formalism developed in the previous section, it is possible to establish a direct connection to superradiance and derive simple analytic expressions.

A. Connection to superradiance

We first notice that, in the stroboscopic description, the relative probabilities of the branching processes are controlled by the small parameter $\beta_m^2 \propto \eta^2$. The most likely event is $|\downarrow, m\rangle \to |\downarrow, m\rangle$ which, however, does not affect M_z. Clearly, only the processes which change m are interesting for the time evolution.

As inferred from Eqs. (19) and (20), the most likely nuclear spin flip is $|\downarrow, m\rangle \to |\downarrow, m-1\rangle$. More precisely, the probability that such a spin flip occurs during the cycle period T is given by:

$$\begin{aligned} T\Gamma_{m\to m-1} &= L_{m-1,m-1}R_{m-1,m} + L_{m-1,m}R_{m,m} \\ &\simeq R_{m-1,m} + L_{m-1,m}, \end{aligned} \tag{22}$$

where in the second line we used $L_{m-1,m-1}, R_{m,m} \simeq 1$ and only kept the terms of order η^2. The presence of two contributions corresponds to spin-flip events taking place either at the right or left contact.

The other types of spin flips have smaller rates. For example, there is also process $|\downarrow, m+1\rangle \to |\downarrow, m+2\rangle$ increasing the nuclear polarization but it has a much smaller rate, $\propto \beta_m^4 \beta_{m+1}^2 \propto \eta^6$. If we neglect them, we find that the nuclear system will slowly depolarize according to Eq. (22). More explicitly:

$$\Gamma_{m\to m-1} \simeq \frac{2\eta^2}{T}[I(I+1) - m(m-1)], \tag{23}$$

where we used $\beta_m \simeq \theta_m/2$ and approximated θ_m by the small η limit of Eq. (4). Such dependence of the depolarization rate on m has the same form of the superradiant decay of an ensemble of N atoms (if $I = N/2$). We then can borrow the known results for the superradiant evolution. In particular, starting from a fully polarized state, $M_z(0) = N/2$, the depolarization time yielding $M_z(t_0) = 0$ is given by

$$t_0 \simeq \frac{\ln(1.6N)}{2N} T/\eta^2, \tag{24}$$

which is in excellent agreement with the stroboscopic dynamics of Fig. 4 (see inset). The following approximate formula for the distribution p_m can also be obtained, considering the limit of large $I = N/2$ and $t \gtrsim T/(2N\eta)$ [25]:

$$p_m(n) \simeq \left(\frac{2I}{I+m}\right)^2 \exp\left[-2I\left(2\eta^2 n + \frac{I-m}{I+m} e^{-4I\eta^2 n}\right)\right]. \tag{25}$$

As shown in Fig. 5, also for the full distribution we find good agreement with superradiance.

B. Electric detection through tunneling events

The evolution of nuclear polarization could be directly observed through the Overhauser field (see, e.g., Ref. [51]). Furthermore, previous proposals related the superradiantlike evolution to a strong enhancement of the transport current through the device [19,21,22]. Unfortunately, this signature is not available here, since there is no applied bias and an electron tunneling into a lead is usually followed by refilling of the shuttle from the same contact.

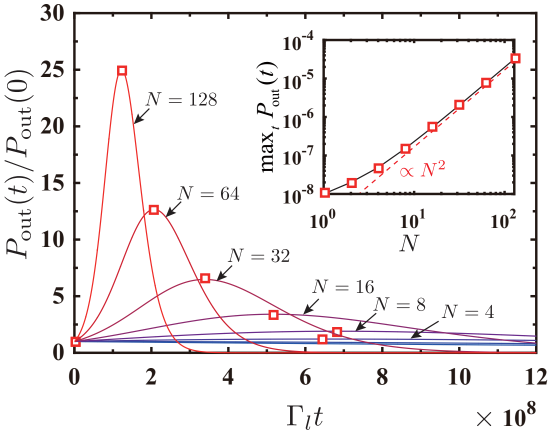

FIG. 6. Tunnel-out probability $P_{\rm out}(t)$, computed for different numbers N of nuclear spins starting from a maximally polarized state $|I, I\rangle$ ($I = N/2$). For the precise definition of $P_{\rm out}(t)$, see Eq. (26). As shown in the inset, the peak value of $P_{\rm out}(t)$ scales quadratically as N^2 when $N \gg 1$. Note that in the main panel $P_{\rm out}(t)$ is normalized by the initial value, thus the peak (square symbols) only scales linearly with respect to N. Parameters used in calculations (in unit of ω_0): $\eta = 10^{-4}$, $\Gamma_l = \Gamma_r = 0.1$, and $t_l = t_r = 30/\Gamma_l$.

For this reason, the electric detection in our setup should rely on monitoring individual tunneling events. While we shall postpone the detailed treatment to Sec. VIII (cf. Figs. 14 and 15), we compute here the probability $P_{\rm out}(nT)$ of observing tunnel events at the left contact during cycle $n+1$:

$$P_{\rm out}(nT) \simeq {\rm Tr}_{\rm nuc}\{\langle\uparrow|\rho_s(nT)|\uparrow\rangle\}, \tag{26}$$

where $\rho_s(nT)$ is the state just after the electron shuttled to the left position. Here we have assumed that, because of a long waiting time, $P_{\rm out}$ is very close to the probability of being in the $|\uparrow\rangle$ state. This state allows the electron to tunnel in the lead, see Fig. 1(b), and shortly after the quantum dot will be refilled in the $|\downarrow\rangle$ state. Detecting this type of events is a standard practice for single-shot read-out of the electron spin [52].

In Fig. 6, we show the time evolution of $P_{\rm out}$ which, as expected, is characterized by a pronounced peak and has a strong dependence on N. The peak value increases quadratically with N (see inset) and occurs at a progressively shorter time, approximately given by Eq. (24). The observation of such a peak would constitute a clear demonstration of the cooperative enhancement of tunneling rates induced by nuclear entanglement. In fact, without nuclear coherence the flip-flop rate would be simply proportional to the number of nuclear spins which can be flipped, $P_{\rm out} \propto M_z(t) - M_z(\infty)$, and would decrease with time. This simple dependence (corresponding to the exponential decay induced by spontaneous emission) is only found in Fig. 6 for the $N = 1$ curve, where the superradiantlike effect cannot take place.

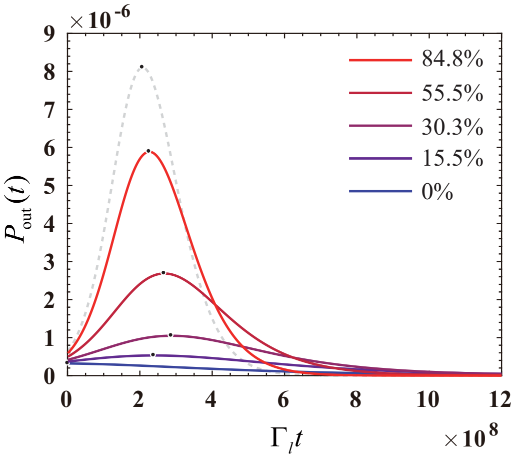

FIG. 7. Effect on $P_{\text{out}}(t)$ of partial nuclear-spin polarization, with $N = 64$. We assume the (properly normalized) initial state in Eq. (27), with $\gamma = 0,\ 20,\ 40,\ 80,$ and 160 (solid curves, from lower to upper). The corresponding percentages of initial spin polarization are also explicitly indicated. The gray dashed curve depicts $P_{\text{out}}(t)$ for a maximally polarized nuclear-spin island. Parameters used in calculations (in unit of ω_0): $\eta = 10^{-4}$, $\Gamma_l = \Gamma_r = 0.1$, and $\Gamma_l t_l = \Gamma_r t_r = 30$.

V. EFFECT OF IMPERFECTIONS AND AN EXTENDED SETUP

As discussed for related proposals [21,22], the enhancement of tunneling rates should be rather robust to various imperfections. We give below some examples, by first relaxing the ideal assumption of a maximally polarized nuclear ensemble. Furthermore, in Sec. V D, we consider a system where nuclear spins are present at both (right/left) operating points. Interestingly, the superradiantlike behavior can still be observed in that configuration, which is relevant for materials with no spinless isotopes (e.g., GaAs).

A. Partial polarization

Our scheme has a preferential direction of polarization (determined by the external magnetic field), so it is best to prepare the initial state by a separate DNP procedure. Efficient DNP schemes were developed [2,16–18,53–57], but maximal polarization is still hard to achieve, e.g., due to the slow cycle frequency [17,55] or nuclear spin relaxation during pumping [16,58]. Here we consider an initial state of the following form:

$$\rho_{\text{nuc}} \propto \exp{[\gamma I^z/N]}, \tag{27}$$

which interpolates between the infinite temperature limit, $\gamma = 0$, and maximal polarization, $|\gamma| \to \infty$. A similar state had been discussed before, with I^z replaced by $(I^z)^2$, to describe narrowing of the nuclear distribution [59]. Since Eq. (27) is diagonal in $|I, m\rangle$, the stroboscopic evolution Eq. (17) can be still applied in each I subspace and the resulting $P_{\text{out}}(t)$ is shown in Fig. 7.

In Fig. 7, no effect of coherence is visible for $\gamma = 0$, thus a certain degree of initial nuclear polarization is necessary. Encouragingly, the superradiantlike peak can be observed under conditions which should not be challenging for standard DNP schemes: A pumping sequence based on transport in the regime of Pauli spin blockade could reach 38%–52% maximum polarization [16], and more than 80% has been achieved with optical pumping [57]. At both levels of spin polarization, Fig. 7 displays a clear superradiantlike peak for $P_{\text{out}}(t)$.

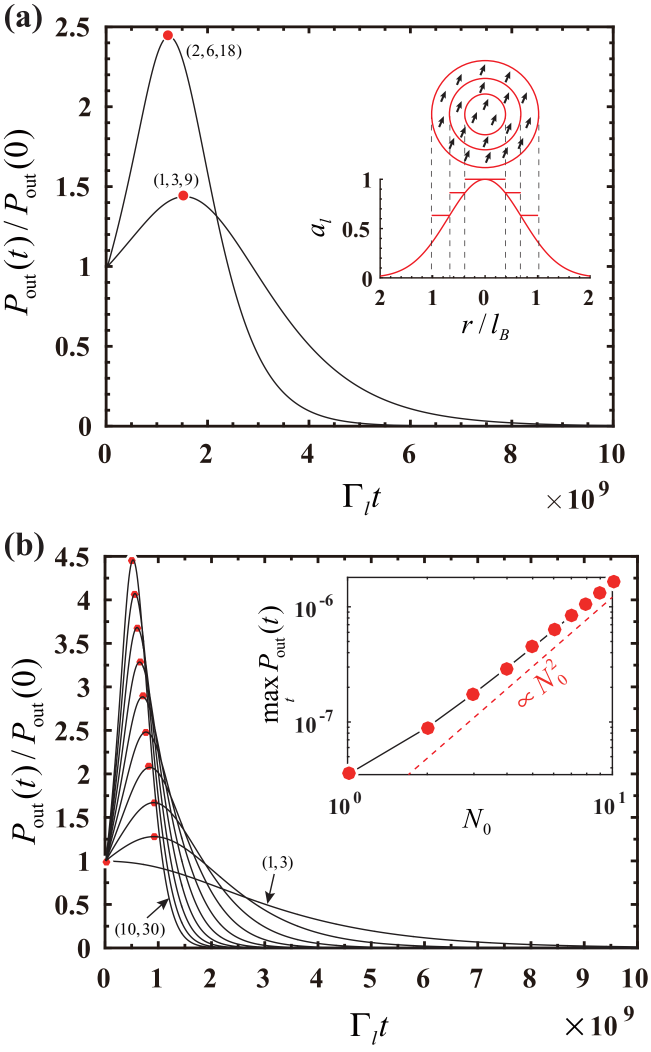

FIG. 8. The tunnel-out probability $P_{\text{out}}(t)$ for a "wedding-cake" model. (a): Three layer model, where (N_0, N_1, N_2) indicates the number of nuclear spins. The values of a_l, see Eq. (28), follow the coarse-graining shown in the inset: $a_1 = 0.91$ and $a_2 = 0.67$. (b): Same as in (a), but calculated including only the first two layers, with $N_0 = 1, 2, \ldots, 10$ and $N_1 = 3N_0$. (Inset) Peak value of $P_{\text{out}}(t)$ as a function of N_0. Other parameters (in unit of ω_0): $\eta = A_0/(2N_d\omega_0) = 10^{-4}$, $\Gamma_l = \Gamma_r = 0.1$, and $t_l = t_r = 30/\Gamma_l$.

B. Inhomogeneous couplings

We consider next the effect of an inhomogeneous hyperfine coupling which, as discussed in Sec. II, depends crucially on the envelope function $\psi(\mathbf{r})$. A common simplification beyond the uniform limit is to introduce a "wedding-cake" coarse-graining [60,61], schematically illustrated in the inset of Fig. 8(a). Under this approach, Eq. (2) is generalized to

$$H_0 = \sum_\sigma \epsilon_\sigma d_\sigma^\dagger d_\sigma + \frac{A}{N_d}\sum_{j=0}^{n_L} a_j \mathbf{I}_j \cdot \mathbf{S}, \tag{28}$$

where n_L is the total number of outer layers and $\mathbf{I}_j$ is the collective angular momentum operator for the jth layer, containing N_j spins. We take $a_0 = 1$ (to recover the previous treatment when $n_L = 0$), while there is some freedom in choosing the values of N_j and $a_{j\neq 0} < 1$, as they depend on the type of confinement.

In Fig. 8(a), we show the evolution of $P_{\rm out}(t)$ obtained solving a three-layers wedding-cake model. Clearly, the peak revealing the coherent enhancement of tunnel rates is visible already for a small number of nuclear spins, and such peak becomes more pronounced by doubling all the N_j. Furthermore, by considering in Fig. 8(b) only two layers, we can compute $P_{\rm out}(t)$ for larger values of N_j and show that the maximum tunnel-out probability still scales quadratically with the number of nuclei (see inset).

These features agree qualitatively with the homogeneous coupling limit. Similar findings about the robustness of the superradiantlike evolution were presented in Ref. [21] which, based on a different approximation, considered rather large nuclear systems (of more than 100 spins). These results indicate that inhomogeneous couplings, although unfavorable, should not prevent observing the effect.

C. Timescales

To estimate the typical timescale of the effect we rely on the depolarization time t_0, approximately given by Eq. (24). Although that expression was derived under the assumption $\eta I \ll 1$, our general formalism is still valid for $\eta I > 1$ (which might be accessible for highly polarized systems), if one relies on the exact eigenstates. In that case, the tunneling rates follow the approximate Eq. (23) only at the beginning of the time evolution, and the initial large enhancement of tunnel rates becomes observable on a timescales shorter than t_0, before it eventually saturates. Therefore Eq. (24) gives a conservative estimate of the interesting timescale.

In general, it is advantageous to work at the lowest Zeeman splitting compatible with the low-temperature and weak-tunneling assumptions, since this choice leads to a larger value of η. Choosing $\omega_0 \simeq 10\,\mu$eV and couplings to the external leads $\sim 1\,\mu$eV (smaller than ω_0), we have an operation cycle $T \sim 1$ ns.[1] We first consider GaAs quantum dots, where $A \simeq 90\,\mu$eV. As we will see in the next Sec. V D, the shuttle still works if both quantum dots are in contact with nuclear spins. Choosing $N_d \simeq 10^5$ and $N = N_d$ gives $\eta = 4.5 \times 10^{-5}$ and $t_0 \simeq 30\,\mu$s, significantly shorter than nuclear dephasing times. For example, a coherence time of 1 ms was reported in Ref. [62] for nuclear spin states in GaAs quantum dots.

For quantum dots based on Si/Ge heterostructures, the smaller values of A and N imply a much longer timescale, $t_0 \simeq 1$ s supposing $\eta \simeq 10^{-6}$ and $N = 5000$. Although maintaining coherence for such extended time is certainly challenging, the restricted geometry for a nuclear-spin island, as well as an engineered uniform-coupling, may lead to a suppression of nuclear spin diffusion through dipolar coupling [63], prolonging nuclear-spin coherence times with respect to GaAs. We also note that extremely long coherence times were demonstrated for nuclear spins of ^{31}P donors embedded in Si, ranging from a few seconds to about 3 hours in bulk samples [64–66] and about 30 seconds in a nanodevice [67]. These results are encouraging for observing the superradiantlike evolution also with group-IV materials.

D. Model with two collective spins

We now address a model more suitable to describe III-V semiconductors, which are materials without spinless isotopes. Then, it is not conceivable to concentrate the nuclear spins at the center of one dot and we consider the following variation of Eq. (2):

$$H_0 = \sum_\sigma \epsilon_\sigma d_\sigma^\dagger d_\sigma + \frac{A_l}{N_l}\mathbf{S}\cdot\mathbf{I}_l + \frac{A_r}{N_r}\mathbf{S}\cdot\mathbf{I}_r, \tag{29}$$

with collective nuclear-spin operators $\mathbf{I}_{l,r}$ at both operating points. N_l and N_r are the number of lattice sites for the left and right quantum dot where, for simplicity, we neglect the effect of inhomogeneous couplings (as discussed in Sec. V B, superradiantlike dynamics should survive inhomogeneity). For definiteness, below we also assume $I_{l,r} = N_{l,r}/2$. Similar to previous discussions, $A_{l,r}$ are time-dependent, through the moving center $x(t)$ of the electron wave function. We take $A_l = 0$ ($A_r = 0$) when the electron resides at the right (left) operating point, which is appropriate if the right and left quantum dots have small overlap.

The presence of two collective spins modifies the eigenstates in a simple way. In particular, if the electron is shuttled to the left position, we define:

$$|\varphi^\pm_{I_l,m_l}, m_r\rangle \equiv |\varphi^\pm_{I_l,m_l}\rangle \otimes |I_r, m_r\rangle, \tag{30}$$

where $|I_r, m_r\rangle$ are the nuclear angular momentum states for the right dot and $|\varphi^\pm_{I_l,m_l}\rangle$ are given by the single-dot eigenstates, Eq. (3), with $A \to A_l$ and $N_d \to N_l$. In a similar way we define the eigenstates $|m_l, \varphi^\pm_{I_r,m_r}\rangle$, when the electron resides at the right operating point. The master equation governing the spin dynamics is also similar to the one discussed in previous sections. In particular, if the electron is shuttled to the left position, Eq. (13) becomes

$$\dot{\rho}_s = -i[H_0, \rho_s] + \Gamma_l \sum_\sigma \big(\mathcal{D}\big[A^l_{\sigma+}\big] + \mathcal{D}\big[\big(A^l_{\sigma-}\big)^\dagger\big]\big)\rho_s, \tag{31}$$

where H_0 is computed with $A_r = 0$ and the Lindblad operators $A^l_{\sigma,\pm} = d_\sigma P^l_\pm$ are as in Eq. (15), except for the projector. At

---

[1] Such a short cycling time T, beneficial to induce a faster superradiantlike dynamics, might become incompatible with the detection of tunnel events, due to the available bandwidth of charge sensing detectors [93,94]. This is a practical difficulty which could be mitigated by extending T, up to the largest values allowed by nuclear coherence. Alternatively, fast shuttling could be interrupted in the course of the superradiantlike evolution, to detect tunnel events (while at the same time reducing the relevant tunnel rates $\Gamma_{l,r}$) or to rely on Overhauser field measurements.

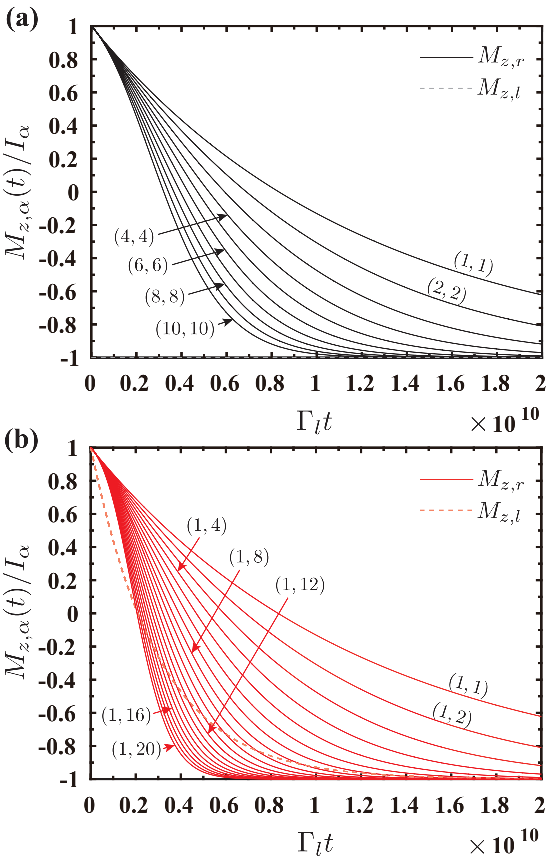

FIG. 9. Time evolution of the nuclear-spin polarization $M_{z,\alpha}$ ($\alpha = l, r$) when both operating points are in contact with nuclear spins. The initial polarization of the two collective spins is antiparallel in (a) and parallel in (b). The numbers (N_l, N_r) in the brackets are the number of nuclear spins at each site. Other parameters (in unit of ω_0): $\eta_l = 2\eta_r = 10^{-4}$, $I_\alpha = N_\alpha/2$, $\Gamma_l = \Gamma_r = 0.1$, and $\Gamma_l t_l = \Gamma_r t_r = 30$.

given values of I_l, I_r,

$$P_\pm^l = \sum_{m_l, m_r} |\varphi^\pm_{I_l,m_l}, m_r\rangle\langle\varphi^\pm_{I_l,m_l}, m_r|. \tag{32}$$

The Lindblad operators $A^r_{\sigma,\pm} = d_\sigma P^r_\pm$ and projectors $P^r_\pm$ at the right operating point are defined in a similar manner, in terms of the $|m_l, \varphi^\pm_{I_r,m_r}\rangle$ eigenstates. They determine the evolution at the right position in a way completely analogous to Eq. (14).

Provided that the above changes to the master equations have been taken into account, the simulation of nuclear-spin polarization dynamics is rather straightforward by using the approaches developed in Sec. III. Examples of numerical results are shown in Fig. 9, where the time-evolution of $M_{z,\alpha}(t) \equiv \text{Tr}\{I^z_\alpha \rho_s(t)\}$ is calculated under two difference initial states. In the first case, the left and right nuclear-spin islands are maximally polarized in opposite directions. Since spin-down electrons entering the shuttle can only lower the nuclear-spin polarization, it is not surprising that left nuclear spins remain essentially frozen. Instead, the right site still shows a superradiantlike dynamics, with the evolution of $M_{z,r}$ strongly affected by N_r.

The bottom panel of Fig. 9 considers an initial state with the two nuclear-spin islands polarized in the same direction. We observe that both $M_{z,l}$ and $M_{z,r}$ achieve a complete reversal, and the system still displays superradiantlike features in the evolution of $M_{z,r}$. To access more easily larger values of N_r, here we assumed $N_l = 1$ and, as a consequence, the evolution of $M_{z,l}$ is essentially independent of N_r and does not show any superradiantlike features. However, we have checked that also with parallel initial polarization the collective enhancement of flip flops occurs for general N_l, N_r.

VI. NON-ADIABATIC CONDITION

We have discussed how the superradiantlike behavior should be observable under a variety of conditions, significantly relaxing the initial assumptions of our setup. However, it is necessary that the shuttling process is sufficiently nonadiabatic. If the transfer from left to right is too slow, an initial $|\downarrow\rangle$ electron will evolve adiabatically into an eigenstate of the hyperfine Hamiltonian, and tunneling processes out of the dot cannot take place. Therefore, in this section, we take a closer look at the shuttling process and discuss the regime of validity of treating it as an ideal quench. Clearly, this approximation is only valid below a certain shuttling time t_f, which we would like to estimate.

To this end, we rewrite $H_0(t)$ in the subspace spanned by $|\uparrow, m-1\rangle$ and $|\downarrow, m\rangle$. This basis defines pseudo-Pauli operators $\tilde{\sigma}_i$, e.g., $\tilde{\sigma}_z = |\uparrow, m-1\rangle\langle\uparrow, m-1| - |\downarrow, m\rangle\langle\downarrow, m|$. Omitting a time-dependent constant, we arrive at

$$H_0(t) = \eta_t \omega_0 \sqrt{I(I+1) - m(m-1)}\tilde{\sigma}_x + \frac{\omega_m(t)}{2}\tilde{\sigma}_z, \tag{33}$$

where

$$\omega_m(t) = \omega_0[1 + \eta_t(2m-1)], \tag{34}$$

and $\eta_t = A(t)/(2N_d\omega_0)$. Assuming that the shuttling takes place with constant velocity, Eq. (12) gives

$$\eta_t = \eta_\text{f} e^{-(t/t_\text{f}-1)^2 L^2/\Delta x^2}, \tag{35}$$

and we initialize the quantum dot in the $t = 0$ ground state $|\varphi^-_{I,m}\rangle \simeq |\downarrow, m\rangle$. After evolving this state according to $H_0(t)$, we compute the probability $\Delta F_m(t_\text{f})$ of finding the quantum dot in the excited state $|\varphi^+_{I,m-1}\rangle$ (with $\eta_{t=t_\text{f}}$ much larger than $\eta_{t=0}$). A numerical evaluation of Eq. (33) is shown in Fig. 10, as function of t_f. The largest probability is obtained for an instantaneous transfer (the quench dynamics of previous sections), giving

$$\Delta F_m(0) \simeq \eta_\text{f}^2[I(I+1) - m(m-1)], \tag{36}$$

which is in direct correspondence to Eq. (23).

Although the initial value Eq. (36) has a strong dependence on m, reflecting the enhancement of spin-flip probability around $m \sim 0$, we see in Fig. 10 that the subsequent decay occurs on a timescale which is only weakly dependent on m. To gain insight into this time-dependence we apply ordinary time-dependent perturbation theory, which is justified by the small value of η_t. We find

$$\Delta F_m(t_\text{f}) \simeq \Delta F_m(0) g\left(\frac{\omega_0 t_\text{f}}{2}\frac{\Delta x}{L}\right), \tag{37}$$

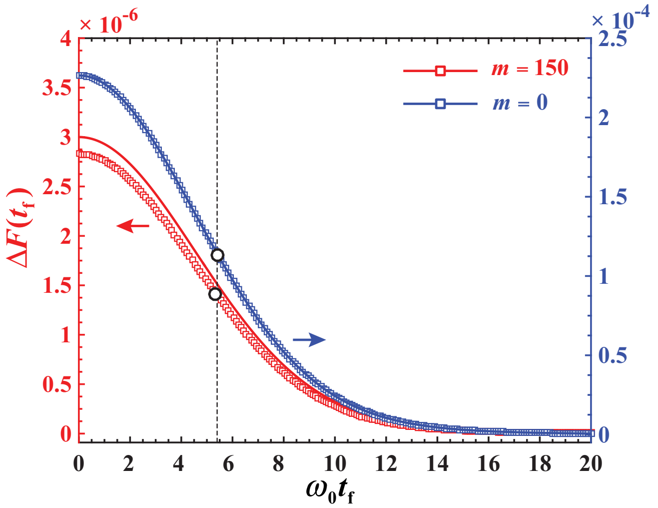

FIG. 10. Probability of finding the quantum dot in the excited state at the end of the shuttling process. Here, the upper (blue) and lower (red) curves are for $m = 0$ and 150, respectively (with $I = N/2 = 150$). Numerical results (squares) are compared to the approximate Eq. (37) (solid lines). The times t_* at which the probability dropped to one half of the initial value are marked by black circles. The vertical line is our estimate of t_*, Eq. (38). We used $\Delta x = L/3$ and $\eta_f^{-1} = 1 \times 10^4$.

where $g(x) = |1 - i\sqrt{\pi}x \exp[-x^2]\text{erfc}(ix)|^2$, with $\text{erfc}(x) = 1 - \text{erf}(x)$ the complementary error function [68]. To derive this expression we supposed $L/\Delta x \gg 1$. However, as shown in Fig. 10, we find that Eq. (37) becomes accurate already at moderate values $L/\Delta x \sim 2$–3.

Importantly, $g(x)$ is independent of m and allows us to identify the relevant timescale as $\omega_0^{-1} L/\Delta x$. For example, setting $\Delta F(t_f) \ll \Delta F(0)/2$, one gets

$$t_f \gg t_* \approx 1.8\omega_0^{-1}\frac{L}{\Delta x}. \tag{38}$$

The physical interpretation of Eq. (38) is rather transparent, after noticing that hyperfine interaction is exponentially suppressed in the first part of the shuttling process. A significant change of the Hamiltonian happens on a distance $\sim\Delta x$, rather than L, which effectively shortens the transfer time by a factor $\sim\Delta x/L$. Therefore the energy is undetermined by an amount $\delta E \sim (t_f \Delta x/L)^{-1}$. If this energy scale is much smaller than the gap ω_0 between ± branches, the probability of being in the excited states is negligible [in agreement with Eq. (38)].

In closing this section, we note that the problem described by Eq. (33) is very similar to the scenario illustrated in Fig. 11, where the shuttling takes place in the presence of a nonuniform magnetic field generated by a micromagnet [69–71]. The main difference is that now the relatively small variation of the magnetic field can be taken as approximately linear (supposing a shuttling process with constant velocity L/t_f). If the time dependence is of the type

$$H_B = \frac{\omega_0}{2}\left[\delta_\perp \frac{t}{t_f}\sigma_x + \left(1 + \delta_\parallel \frac{t}{t_f}\right)\sigma_z\right], \tag{39}$$

where $|\delta_{\perp,\parallel}| \ll 1$, the probability of being in the excited state at the end of the transfer process (starting from $|\downarrow\rangle$) can be computed as follows:

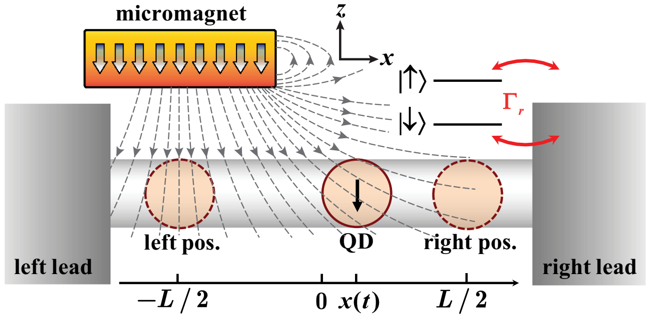

FIG. 11. Schematics of an alternative shuttling setup. Here there are no nuclear spins but the electron shuttles through the inhomogeneous field of a nearby micromagnet. In addition, a large homogeneous field is applied along z.

$$\Delta F(t_f) \simeq \frac{\delta_\perp^2}{4}\frac{\sin^2(\omega_0 t_f/2)}{(\omega_0 t_f)^2/4}, \tag{40}$$

giving the characteristic timescale

$$t_* \sim 2.8\omega_0^{-1}. \tag{41}$$

We see that also in this case t_* is determined by the Zeeman splitting. For $t_f \gg t_*$, the shuttling process is slow and allows the spin to adjust to the instantaneous field. On the other hand, if $t_f \lesssim t_*$, the electron will have a probability $\gtrsim \frac{1}{8}\delta_\perp^2$ to be excited at the end of the transfer process and, with a bias configuration like in Fig. 11, can tunnel out of the quantum dot.

In summary, we find that the typical timescale of shuttling processes inducing an electron spin flip is given by the inverse Zeeman energy: both for the nuclear-spin island and the micromagnet a shuttling time of order ω_0^{-1} has an effect similar to the instantaneous transfer [see Eqs. (38) and (41), respectively]. For a Zeeman splitting of $\sim 10\,\mu$eV, Eq. (38) gives a nonadiabatic shuttling time of order 200 ps. Such a fast manipulation of charge states was already demonstrated in double quantum dots [72,73].

VII. SHUTTLING VERSUS STATIONARY CONFIGURATIONS

The superradiantlike dynamics of nuclear spins in single quantum dots was discussed in Refs. [21,22], where stationary configurations were considered (with no shuttling). We would like to highlight in this section what are the main differences and potential advantages of the shuttling configuration. Especially, the scheme analyzed in Ref. [21] considers an ordinary quantum dot in the weak tunneling regime, with a simple level structure and normal leads. That proposal represents an attractive option, but we find that the superradiantlike transport features disappear in a revised theoretical description, suggesting that a nonadiabatic process analogous to fast shuttling is necessary.

To clarify this point, we consider in detail the transport model illustrated in the inset of Fig. 12. Since the position of the dot is kept fixed, the Hamiltonian is simply given by Eq. (1), with time-independent tunneling amplitudes and

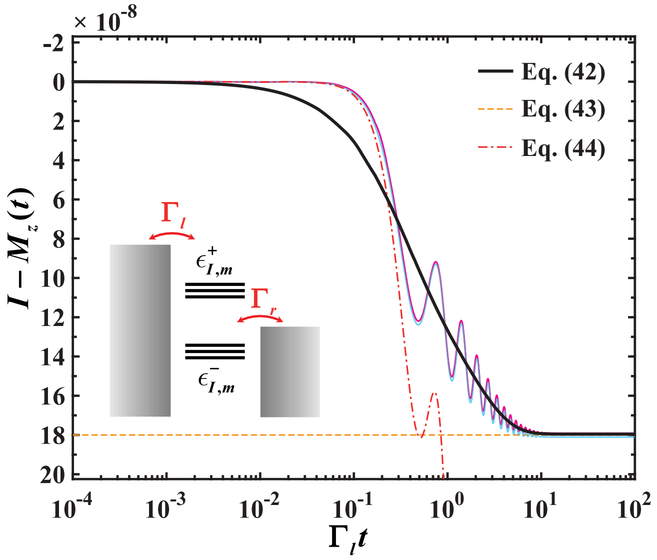

FIG. 12. Nuclear-spin polarization versus time in a stationary quantum dot configuration (see inset). The black solid curve shows M_z from solving the Lindblad master equation, Eq. (42). The thin blue curve is from Eq. (A6), i.e., without performing the RWA and taking into account the Lamb shift $\Delta_{\rm LS}$ (the thin magenta curve shows the small effect of setting $\Delta_{\rm LS} = 0$). The red dash-dotted curve is the more approximate evolution Eq. (44). Parameters used in the calculations (in unit of ω_0): $N = 12$, $I = N/2$, $\eta = 10^{-4}$, $\Gamma_l = \Gamma_r = 0.1$, $\mu_l = 2$, $\mu_r = 0$, and $\Lambda = 10^3$ [cf. Eq. (A9)].

hyperfine coupling strength. An external bias is applied, with the $\epsilon^+_{I,m}$ levels lying in the transport window. The main simplifications with respect to Ref. [21] are that we restrict ourselves to a uniform hyperfine coupling and large Zeeman splitting, such that we can avoid including a dynamical compensation of the longitudinal Overhauser field (along z). We derive the master equation as in Sec. III (and Appendix A), obtaining

$$\dot{\rho}_s = -i[H_0, \rho_s] + \sum_\sigma (\Gamma_r \mathcal{D}[A_{\sigma+}]\rho_s + \Gamma_l \mathcal{D}[A^\dagger_{\sigma+}]\rho_s + (\Gamma_r + \Gamma_l)\mathcal{D}[A^\dagger_{\sigma-}]\rho_s), \tag{42}$$

where the Lindblad operators are given in Eq. (15). A numerical example of the typical nuclear polarization dynamics (starting with an empty quantum dot, $|0\rangle \otimes |I, I\rangle$) is presented in Fig. 12.

The most remarkable feature of of Fig. 12 is the small change in M_z, which is in contrast to the full polarization reversal predicted for superradiantlike dynamics. The stationary state is determined by the special form of the Lindblad operators $A_{\sigma\pm}$, which involve projectors on the $\pm$ bands. Therefore the $|\varphi^-_{I,m}\rangle$ eigenstates are stationary solutions of the master equation, inhibiting further dynamics. According to Eq. (42), the nuclear spin bath is unable to remove the Coulomb blockade and, once the quantum dot is occupied in the $-$ band, there are no further spin flips affecting the nuclear-spin polarization.

Based on Eq. (42), we can give an approximate expression of the small polarization loss from a rate equation analysis, using the fact that η is small. This approach is described in detail in Appendix B and here we only cite the final result for the stationary value. For $I = N/2$,

$$M_z(t \to \infty) \simeq \frac{N}{2}\left(1 - 2\eta^2 \frac{2\Gamma_l + \Gamma_r}{\Gamma_l + \Gamma_r}\right), \tag{43}$$

showing that the depolarization is indeed small when $\eta \ll 1$. We have also extended the above analysis by evaluating the higher order corrections to M_z, see Eq. (B8).

To check that the behavior is not an artifact of the RWA between the $\pm$ bands, we have also integrated numerically Eq. (A6), which only relies on the second-order Born-Markov approximation (justified in the weak-tunneling regime $\Gamma_{l,r} \ll \omega_0$). As expected, this treatment displays a short-time oscillatory dynamics absent under RWA. Otherwise, as shown in Fig. 12, the two approaches agree on the general features of the time-dependence and, most importantly, on the small change of the spin polarization.

A superradiantlike master equation [21,22] can be obtained from Eq. (42) by neglecting the hyperfine interaction in the dissipator:

$$\dot{\rho}_s \simeq -i[H_0, \rho_s] + \Gamma_r \mathcal{D}[d_\uparrow]\rho_s + \Gamma_l \mathcal{D}[d^\dagger_\uparrow]\rho_s + (\Gamma_r + \Gamma_l)\mathcal{D}[d^\dagger_\downarrow]\rho_s, \tag{44}$$

which dramatically changes the long-time behavior. A numerical solution of Eq. (44) is shown in Fig. 12, where the saturation of M_z is not observed in this case. However, we stress that Eq. (44) involves an additional approximation with respect to Eq. (42).

To understand the disagreement between the two master equations we note that Eq. (44) can be justified at any given timescale when the hyperfine coupling A is sufficiently small. In that limit, indeed $A_{\uparrow,+} \simeq d_\uparrow$ and $A_{\downarrow,-} \simeq d_\downarrow$ [see after Eq. (15)]. However, when $A \to 0$, it also happens that the rate of flip-flop processes decreases quickly, being proportional to A^2. Correspondingly, the predicted timescale of the superradiantlike evolution grows like $\propto A^{-2}$. On this diverging timescale, the small difference in propagators between Eqs. (44) and (42) leads to important deviations. From Fig. 12, we conclude that the threshold time for Eq. (44) [i.e., the time after which it becomes inaccurate] must be shorter than the predicted superradiantlike timescale.

In the light of these discussions, one can appreciate better the crucial role played in our proposal by the nonadiabatic shuttling processes, which allows to overcome the blockaded regime and induce the desired superradiantlike evolution. Another stationary setup was put forward in Ref. [22] which, however, requires the fabrication of ferromagnetic leads [74–78].

VIII. STOCHASTIC EVOLUTION

We devote this last section to a treatment of fluctuations in the electrical detection process. As we already mentioned (see Sec. IV B), the presence of nuclear-spin coherence could be inferred through cooperatively enhanced tunneling rates, detected through charge sensing. An example of a specific setup is shown in Fig. 13, where we include two quantum point contacts at the left/right operation point, to allow detecting individual tunneling events. In such a setup, a typical measurement would involve monitoring the quantum dot

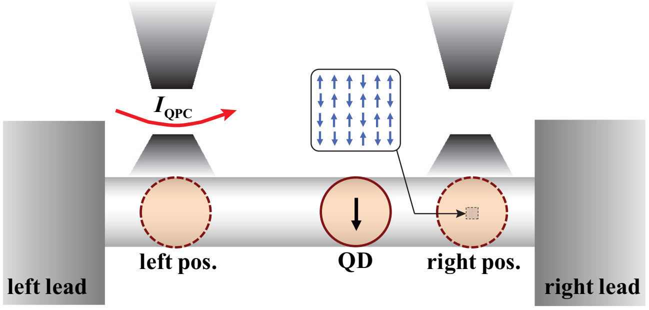

FIG. 13. Schematics of the electron shuttle with two nearby charge sensors, e.g., quantum point contacts (QPC). The sensors can perform nondemolition measurements on the quantum dot occupation n_{dot} when the dot is moved to the respective proximal positions.

occupation and the superradiantlike dynamics will be reflected by the statistical properties of tunnel events.

To address this type of evolution it is convenient to adopt a quantum-jump description of the master equation [79,80]. Following the standard prescription, the following collapse operators are introduced for Eq. (13):

$$C_{l,1} = \sqrt{\Gamma_l} d_\uparrow, \quad C_{l,2} = \sqrt{\Gamma_l} d_\downarrow^\dagger, \tag{45}$$

and the collapse operators for Eq. (14) read

$$C_{r,1} = \sqrt{\Gamma_r} A_{\uparrow+}, \quad C_{r,2} = \sqrt{\Gamma_r} A_{\downarrow+}, \tag{46}$$

$$C_{r,3} = \sqrt{\Gamma_r} A_{\uparrow-}^\dagger, \quad C_{r,4} = \sqrt{\Gamma_r} A_{\downarrow-}^\dagger. \tag{47}$$

In the periods between quantum jumps the electron and nuclear spins evolve according to an effective non-Hermitian Hamiltonian, $H_z - i/2 \sum_m C_{l,m}^\dagger C_{l,m}$ or $H_0 - i/2 \sum_m C_{r,m}^\dagger C_{r,m}$ depending on the quantum dot's position. Since the jump operators in Eqs. (45)–(47) correspond to projective measurements induced by the coupling with the left and right leads, they provide a direct connection between individual trajectories and the signal of charge sensors monitoring the quantum dot.

Figure 14 illustrates a typical trajectory from the Monte Carlo wave-function simulation. We show in panel (a) the evolution of the quantum dot's occupation, characterized by a series of tunneling events where the electron jumps to the right/left contact and is reloaded from it on a timescale set by $\Gamma_{l,r}$ (see the inset). An important feature is the visible change in frequency of tunneling events, which are much more rare at the beginning and the end of time evolution. The increase of frequency at intermediate times (despite the smaller number of nuclear spins which can be flipped) reflects the enhancement of tunnel rate induced by the nuclear coherence.

A second important observation, illustrated in panel (b), is the direct correspondence of tunnel events to the quantum jumps in the nuclear-spin polarization. As seen, a change $|\Delta M_z| \simeq 1$ is associated with tunnel events occurring at both (left/right) contacts, Although, in principle, some of the tunneling events might leave M_z unchanged, these instances are very unlikely (their probability is suppressed by an additional factor η^2, because they involve two electron-nuclear flip flops instead of one) and do not occur in Fig. 14. Thus one can rely on charge measurements to monitor the nuclear-spin polarization. Finally, we show in panel (c) that the ensemble-averaged nuclear-spin polarization coincides with the master equation treatment.

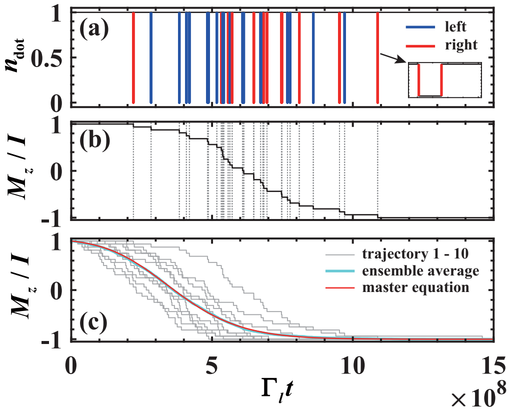

FIG. 14. Charge sensing and nuclear-spin polarization dynamics from the Monte Carlo wave-function (MCWF) simulation. (a) Quantum dot occupation n_{dot} as a function of time for a representative MCWF trajectory. The blue (red) color marks tunneling events that happen when the dot is at the left (right) operating point. (b) Nuclear-spin polarization M_z/I (black solid) as a function of time, for the same trajectory of panel (a). The vertical dashed lines highlight the correspondence between jumps in polarization and tunneling events. (c) M_z from an ensemble average over 100 MCWF trajectories (thick light-blue). The red thin curve is obtained from solving the stroboscopic evolution Eq. (17) with an initial distribution $p_m(0) = \delta_{m,I}$. The light gray curves shows the M_z dynamics from 10 MCWF trajectories from the ensemble. Parameters used in the calculations (in unit of ω_0): $N = 32$, $I = N/2$, $\eta = 10^{-4}$, $\Gamma_l = \Gamma_r = 0.1$, and $t_l = t_r = 300$.

To quantify more precisely the occurrence of tunnel events, we consider a coarse-grained evolution over larger time intervals $\Delta t \gg T$, i.e., spanning many shuttling cycles. Since a trajectory k (with $k = 1, 2, \ldots, N_{\text{traj}}$) is characterized by a series of random times $t_j^{(k)}$ ($j = 1, 2, \ldots$) at which the electron tunnels out of the quantum dot, we introduce $\Delta n_{\text{dot}}^{(k)}(m)$ as follows:

$$\Delta n_{\text{dot}}^{(k)}(m) = \int_{(m-1)\Delta t}^{m\Delta t} dt \sum_j \delta\big(t - t_j^{(k)}\big), \tag{48}$$

which counts the number of narrow spikes in n_{dot} (see Fig. 14) within the mth time interval. Operationally, the $t_j^{(k)}$s are detected from signal blips at the charge sensors. The average number during such mth subperiod is

$$\overline{\Delta n_{\text{dot}}(m)} = \frac{1}{N_{\text{traj}}} \sum_{k=1}^{N_{\text{traj}}} \Delta n_{\text{dot}}^{(k)}(m) \tag{49}$$

and the fluctuation is given by

$$\sigma_{\text{dot}}^2(m) = \overline{\Delta n_{\text{dot}}(m)^2} - \overline{\Delta n_{\text{dot}}(m)}^2. \tag{50}$$

The evolution of these quantities with time, obtained numerically from a MCWF simulations of 100 trajectories, is shown in Fig. 15(a). For each subinterval, the distribution of tunneling events can also be extracted by direct histogram,

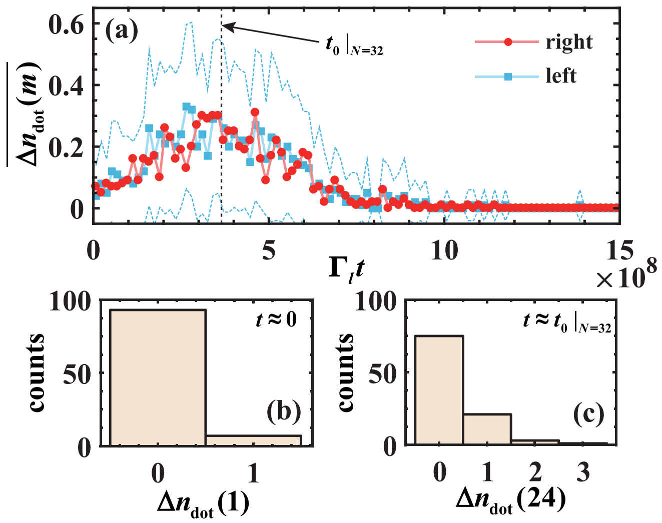

FIG. 15. Statistics of $\Delta n_{\rm dot}(m)$ from the 100 MCWF trajectories of Fig. 14. We consider a coarse-grained evolution with 100 intervals ($m = 1, 2, \dots, 100$). (a) Evolution of the average value, defined in Eq. (49) and resolved between the left (light-blue squares) and right (red dots) contacts. The region bounded by the two blue dashed curves indicates the fluctuations of $\Delta n_{\rm dot}(m)$ at the left contact, with the upper and lower bounds (dashed lines) given by $\overline{\Delta n_{\rm dot}(m)} \pm \sigma_{\rm dot}(m)/2$ [see Eq. (50)]. (b) and (c) show the distribution of $\Delta n_{\rm dot}(m)$ at the initial and intermediate stage evolution, respectively. The time assumed in (c) is marked in (a) by a vertical dashed line. The two lower panels refer to the right contact, while the histograms of the left contact are almost identical.

with two examples shown in panels (b) and (c). Since we are dealing with a transient process, the form of the distribution evolves in time and, compared to the initial stage, develops an elongated tail around $t \sim t_0$ [see Eq. (24)]. This dependence leads to the maximum in $\overline{\Delta n_{\rm dot}(m)}$ observed in panel (a). The increased frequency of tunnel events is also accompanied by stronger fluctuations in $\Delta n_{\rm dot}(m)$, reflecting the broad superradiantlike statistical distribution discussed in Fig. 5.

An interesting observation from Fig. 15 is that the behavior of the right and left contacts is basically equivalent (we have checked that this property holds to leading order in η^2). Finally, we note that a detailed monitoring tunnel events might not be necessary. At variance with previous proposals [19,21,22] here we do not apply a bias and there is zero average current flowing through the device [see, e.g., Fig. 15(a), displaying a balanced number of tunnel in/out events at each contact]. Nevertheless, the evolution of $\overline{\Delta n_{\rm dot}(m)}$ reflects enhanced charge fluctuations at intermediate times $t \sim t_0$. Therefore an analysis of the time-dependent charge noise at either one of the contacts should be able to reveal the coherent enhancement of tunnel rates induced by nuclear spins.

IX. CONCLUSION

In this work, we have analyzed the combined electron-nuclear spin dynamics in a shuttling device. We have shown that, under suitable conditions, it is possible to generate quantum coherence in the nuclear spin system through collective electron-nuclear flip-flop processes, and the superradiantlike evolution is reflected in a large enhancement of electron tunneling rates.

In general, since the ideal evolution proceeds through a cascade of Dicke states, superradiantlike dynamcs might find useful applications in metrology [81,82]. The most favorable states are those with nearly zero-nuclear spin polarization, which also yield the largest enhancement of spin-flip tunneling, thus can most easily identified. Dicke states are also interesting for quantum networking, see Ref. [83] and references therein for specific algorithms on teleportation, telecloning, and quantum secret sharing.

While we have focused here on quantum dots, which is partially motivated by recent experimental progress on electron shuttling [39,40], the same ideas could be relevant to other platforms, like donor impurities with high-spin nuclei [84–87]. In that case, it would be important to assess the influence of quadrupolar interaction and strain [88–90].

Finally we note that an important assumption of our setup and of previous proposals [21,22] is a weak-tunneling condition. Since efficient stationary DNP schemes were developed with tunneling rates comparable or larger than the singlet-triplet splitting of a double quantum dot [16], superradiantlike schemes in the strong tunneling regime might deserve further investigation.

ACKNOWLEDGMENTS

We thank W. A. Coish, G. Burkard, and Wen Yang for helpful discussions. S. Chesi acknowledges support from the National Key Research and Development Program of China (Grant No. 2016YFA0301200), NSFC (Grants No. 11574025, No. 11750110428, No. 1171101295, and No. 11974040), and NSAF (Grant No. U1930402). Y.-D. Wang acknowledges support from NSFC (Grant No. 11947302) and MOST (Grant No. 2017FA0304500).

APPENDIX A: MASTER EQUATION OF THE QUANTUM DOT

We present here the derivation of the master equation describing the stationary quantum dot, i.e., based on Eq. (1) after tracing out the leads degrees of freedom. Restricting ourselves to the weak-tunneling regime, we adopt the standard second-order Born-Markov approximation [91,92]:

$$\dot{\tilde{\rho}}_s(t) = -\int_0^\infty d\tau \mathrm{Tr}_b\{[\tilde{H}_T(t), [\tilde{H}_T(t-\tau), \tilde{\rho}_s(t) \otimes \rho_b]]\}, \tag{A1}$$

where $\rho_s(t) = \mathrm{Tr}_b\{\rho(t)\}$ is the reduced density matrix of the quantum dot, $\mathrm{Tr}_b\{\dots\}$ is the partial trace over the leads, and ρ_b is the reduced density matrix of the leads with given chemical potentials μ_α [see Eq. (9)]. The tilde indicates operators in the interaction picture, $\tilde{O}(t) = e^{i(H_0+H_b)t} O(t) e^{-i(H_0+H_b)t}$.

To evaluate Eq. (A1) more explicitly, we use the exact eigenstates of H_0 given in Eq. (3). In this section, we indicate them as $|\xi\rangle$ (with energy ϵ_ξ). In particular, we introduce the spectral decomposition $d_\sigma^\dagger = \int_{-\infty}^{\infty} d\omega d_\sigma^\dagger(\omega)$, where [91]

$$d_\sigma^\dagger(\omega) = [d_\sigma(\omega)]^\dagger = \sum_{\xi,\xi'} |\xi\rangle\langle\xi|d_\sigma^\dagger|\xi'\rangle\langle\xi'|\delta(\omega - \epsilon_\xi). \tag{A2}$$

It is then straightforward to write H_T in the interaction picture and obtain

$$\dot{\tilde{\rho}}_s(t) = \sum_\sigma \int d\omega d\omega' \{\Gamma_{\rm out}(\omega)[d_\sigma(\omega)\tilde{\rho}_s(t), d_\sigma^\dagger(\omega')] + \Gamma_{\rm in}(\omega')[d_\sigma^\dagger(\omega')\tilde{\rho}_s(t), d_\sigma(\omega)]\}e^{i(\omega'-\omega)t} + \text{H.c.}, \tag{A3}$$

where we defined

$$\Gamma_{\rm out}(\omega) = \sum_{\alpha k} \int_0^\infty d\tau e^{i(\omega-\varepsilon_{\alpha k})\tau} |T_{\alpha k}|^2 (1 - f_\alpha(\varepsilon_{\alpha k})),$$
$$\Gamma_{\rm in}(\omega) = \sum_{\alpha k} \int_0^\infty d\tau e^{-i(\omega-\varepsilon_{\alpha k})\tau} |T_{\alpha k}|^2 f_\alpha(\varepsilon_{\alpha k}). \tag{A4}$$

Note that in Eq. (A2) the argument of the delta function contains ϵ_ξ instead of the transition frequency $\epsilon_\xi - \epsilon_{\xi'}$, simply because $|\xi'\rangle$ corresponds to an empty quantum dot and $\epsilon_{\xi'} = 0$. After going back to the Schrödinger picture, the integrals over frequencies in Eq. (A3) can be evaluated by introducing the operators $\Gamma_{\rm in/out}(H_0)$. It is easy to see that $\int d\omega \Gamma_{\rm out}(\omega) d_\sigma(\omega) = d_\sigma \Gamma_{\rm out}(H_0)$ and similarly for other integrals of this type. Furthermore, introducing the Hermitian operators $\gamma_{\rm in/out}, \Delta_{\rm in/out}$:

$$\Gamma_{\rm in/out}(H_0) \equiv \frac{\gamma_{\rm in/out}}{2} + i\Delta_{\rm in/out}, \tag{A5}$$

and using that $\Delta_{\rm in/out}$ are approximately equal [$\Delta_{\rm in/out} \simeq \Delta_{\rm LS}$, see Eq. (A9) below], we arrive at

$$\dot{\rho}_s = -i[H_0, \rho_s] + \sum_\sigma \left\{ \left[d_\sigma \left(\frac{\gamma_{\rm out}}{2} + i\Delta_{\rm LS} \right) \rho_s, d_\sigma^\dagger \right] + \left[\left(\frac{\gamma_{\rm in}}{2} + i\Delta_{\rm LS} \right) d_\sigma^\dagger \rho_s, d_\sigma \right] + \text{H.c.} \right\}. \tag{A6}$$

We now give the explicit expressions of $\gamma_{\rm in/out}$ and $\Delta_{\rm LS}$, where as usual we transform $\sum_k \to \int d\varepsilon$ and compute the integrals assuming constant density of states and tunnel amplitudes. In this way, we obtain

$$\gamma_{\rm in} = \sum_\alpha \Gamma_\alpha \theta(\mu_\alpha - H_0), \quad \gamma_{\rm out} = \sum_\alpha \Gamma_\alpha \theta(H_0 - \mu_\alpha), \tag{A7}$$

where the tunnel rates Γ_α are given in Eq. (11). For the Lamb-shift terms, we have

$$\Delta_{\rm in} = \sum_\alpha \Gamma_\alpha \left(\text{P} \int_{\mu_\alpha - \Lambda}^{\mu_\alpha} \frac{d\varepsilon}{2\pi} \frac{1}{\varepsilon - H_0} \right),$$
$$\Delta_{\rm out} = \sum_\alpha \Gamma_\alpha \left(\text{P} \int_{\mu_\alpha}^{\mu_\alpha + \Lambda} \frac{d\varepsilon}{2\pi} \frac{1}{H_0 - \varepsilon} \right), \tag{A8}$$

where we supposed the α lead to have a bandwidth 2Λ around its chemical potential μ_α. In the limit of large Λ,

$$\Delta_{\rm in/out} \simeq \Delta_{\rm LS} = \sum_\alpha \frac{\Gamma_\alpha}{2\pi} \ln\left(\frac{|\mu_\alpha - H_0|}{\Lambda} \right). \tag{A9}$$

Interestingly, the choice of the cutoff does not affect the evolution of ρ_s. In fact, by changing Λ, the right-hand side of Eq. (A6) is modified by a term proportional to

$$\sum_\sigma ([d_\sigma \rho_s, d_\sigma^\dagger] + [d_\sigma^\dagger \rho_s, d_\sigma] - \text{H.c.}) = \sum_\sigma [\rho_s, \{d_\sigma^\dagger, d_\sigma\}], \tag{A10}$$

which is obviously zero since $\{d_\sigma^\dagger, d_\sigma\} = 1$.

So far, the main result of this section is Eq. (A6), which with uniform hyperfine coupling and fixed total angular momentum I can be evaluated for a relatively large nuclear system. An example is given in Fig. 12 of the main text. We emphasize that Eqs. (A1) and (A6) are essentially equivalent, since the derivation of Eq. (A6) does not involve further approximations, except for standard assumptions on the leads density of states and tunnel amplitudes. Furthermore, we did not perform yet a rotating-wave approximation. For this reason, the dissipation of Eq. (A6) is not in the Lindblad form, and small unphysical effects can appear during the time evolution.

To obtain a master equation of the Lindblad type, we perform a partial rotating-wave approximation on Eq. (A6). We can also drop the Lamb shift, which usually has a small effect (see Fig. 12). To neglect fast-oscillating terms, we first express $\gamma_{\rm in/out}$ in terms of the projectors $P_\pm$ on the two well-separated bands of states. For example, for the bias configuration shown in the inset of Fig. 12,

$$\gamma_{\rm in} = (\Gamma_l + \Gamma_r)P_- + \Gamma_l P_+, \quad \gamma_{\rm out} = \Gamma_r P_+. \tag{A11}$$

Then, the projected fermionic operators $A_{\sigma\pm}$ [defined in Eq. (15)] naturally appear in the master equation Eq. (A6). We can also use the fact that, since we always omit doubly occupied states, the $A_{\sigma\pm}$ provide a decomposition of the d_σ operators: $d_\sigma = A_{\sigma+} + A_{\sigma-}$. Finally, based on the large energy separation between the P_+ and P_- subspaces, we neglect in Eq. (A6) the cross-terms involving two bands simultaneously (i.e., the terms containing both $A_{\sigma+}$ and $A_{\sigma-}$). This treatment lead to Eqs. (14) and (42) of the main text, where the dissipator is indeed of Lindblad type.

APPENDIX B: RATE EQUATIONS AND SMALL-η EXPANSION

An even simpler description of the quantum dot dynamics is through rate equations. For our systems, the description through rate equations gives results which are in agreement with more sophisticated treatments. In some cases, they are even equivalent to the evolution based on a full master equation. For example, a detailed analysis of Eq. (42) shows that for the initial state $|0\rangle \otimes |I, I\rangle$ the density matrix remains diagonal in the basis of the eigenstates. We will then consider the rate equations following Eq. (42). By neglecting the coherence between all the eigenstates $|\xi\rangle$ of H_0, i.e., assuming $\langle\xi|\rho_s|\xi'\rangle \simeq P_\xi \delta_{\xi\xi'}$, we obtain

$$\begin{aligned}
\dot{P}_{+,m} &= \Gamma_l\big(\alpha_m^2 P_{0,m} + \beta_m^2 P_{0,m+1}\big) - \Gamma_r P_{+,m},\\
\dot{P}_{-,m} &= (\Gamma_r + \Gamma_l)\big(\alpha_{m-1}^2 P_{0,m} + \beta_{m-1}^2 P_{0,m-1}\big),\\
\dot{P}_{0,m} &= \Gamma_r\big(\alpha_m^2 P_{+,m} + \beta_{m-1}^2 P_{+,m-1}\big)\\
&\quad - \big(2\Gamma_l + \Gamma_r\beta_m^2 + \Gamma_r\alpha_{m-1}^2\big)P_{0,m},
\end{aligned} \tag{B1}$$

where $P_{\pm,m} = \langle \varphi^{\pm}_{I,m} | \rho_s | \varphi^{\pm}_{I,m} \rangle$ and $P_{0,m} = \langle 0, m | \rho_s | 0, m \rangle$ are respectively the populations of the occupied and empty quantum dot. We recall here the notation $|0, m\rangle = |0\rangle \otimes |I, m\rangle$ and that $\alpha_m = \cos(\theta_m/2)$, $\beta_m = \sin(\theta_m/2)$, with the mixing angle given in Eq. (4).

The physical interpretation of Eq. (B1) is rather transparent, as the various contributions on the right-hand side can be associated to spin-conserving and spin-flipping tunnel events to/from the quantum dot: the terms proportional to β_m^2 correspond to tunneling events accompanied by a flip-flop process of the electron and nuclear spins. For such processes, the rates are suppressed by the square amplitude of the spin-flipped component in the quantum-dot eigenstates, see Eq. (3). Instead, the terms proportional to α_m^2 are associated to processes when the nuclear spin flip does not take place.

To gain analytical insight into the rate equations (B1) and obtain a simple analytical expression for the nuclear-spin polarization $M_z(t)$, we take advantage of the small parameter η and expand the populations perturbatively:

$$P_{s,m} = P^{(0)}_{s,m} + P^{(2)}_{s,m} + P^{(3)}_{s,m} + \cdots , \tag{B2}$$

where $P^{(k)}_{s,m}$ is proportional to η^k (as we will see below, the $O(\eta)$ term is missing). The lowest-order result is obtained taking $\alpha_m^2 \simeq 1$ and $\beta_m^2 \simeq 0$ and gives the evolution in the absence of hyperfine interaction. For an initial state $\rho_s(0) = |0, I\rangle\langle 0, I|$, it is easy to obtain

$$\begin{aligned} P^{(0)}_{+,I}(t) &= \sqrt{\frac{\Gamma_l}{\Gamma_l + \Gamma_r}} e^{-(\Gamma_l+\Gamma_r)t} \sinh \sqrt{\Gamma_l(\Gamma_l + \Gamma_r)}t, \\ P^{(0)}_{-,I}(t) &= 1 - e^{-(\Gamma_l+\Gamma_r)t} \cosh \sqrt{\Gamma_l(\Gamma_l + \Gamma_r)}t, \end{aligned} \tag{B3}$$

while $P^{(0)}_{0,I} = 1 - P^{(0)}_{+,I} - P^{(0)}_{-,I}$ and all other $P^{(0)}_{s,m}$ are zero. To obtain the higher-order contributions, we consider the expansion of β_m^2 (note that $\alpha_m^2 = 1 - \beta_m^2$):

$$\beta_m^2 = g^{(2)}_m \eta^2 + g^{(3)}_m \eta^3 + \cdots , \tag{B4}$$

where $g^{(2)}_m = I(I+1) - m(m+1)$ and $g^{(3)}_m = -2(2m+1)g^{(2)}_m$. We see that the first correction is indeed of order η^2. More precisely, since $g^{(j)}_m \sim I^j$, the expansion parameter is $I\eta$. If we take $I \sim N$, the condition of validity becomes $AN/N_d \ll \omega_0$. By making use of Eqs. (B3) and (B4) in the rate equations, it is straightforward to obtain the equation of motions for $P^{(2)}_{s,m}$ and $P^{(3)}_{s,m}$. For example, defining $P^{(k)}_m = P^{(k)}_{0,m} + P^{(k)}_{+,m} + P^{(k)}_{-,m}$, we obtain the compact equation (with $j = 2, 3$):

$$\dot{P}^{(j)}_{I-1}(t) = -\dot{P}^{(j)}_I(t) = \eta^j g^{(j)}_{I-1} \Gamma_l P^{(0)}_{0,I}(t). \tag{B5}$$

It is also possible to apply the perturbative solution to the nuclear-spin polarization:

$$M_z(t) = \sum_m m P_{0,m} + \sum_{\sigma,s,m,m'} m \left| \langle \sigma, m | \varphi^s_{I,m'} \rangle \right|^2 P_{s,m'}. \tag{B6}$$

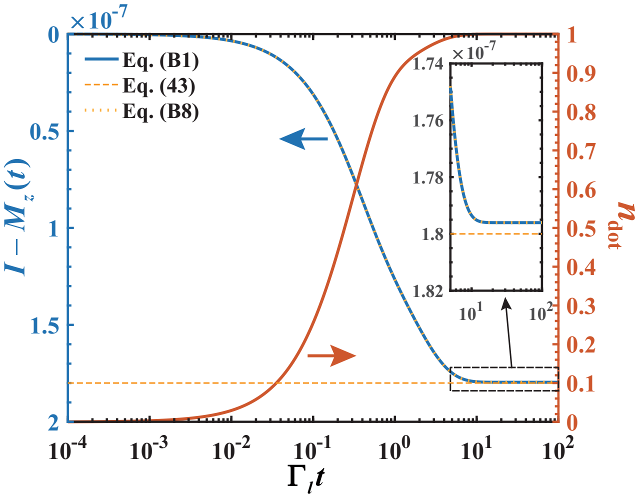

FIG. 16. Nuclear-spin polarization dynamics from the rate equations Eq. (B1). The approximated results, i.e., dashed and dotted curves, agree well with the exact numerics (blue solid curve). The orange solid curve (right scale) is the corresponding quantum dot occupation, $n_{\rm dot} = \langle d^\dagger_\uparrow d_\uparrow + d^\dagger_\downarrow d_\downarrow \rangle$, which quickly saturates to $n_{\rm dot} = 1$. Parameters used in the calculations (in unit of ω_0): $N = 12$, $I = N/2$, $\eta = 10^{-4}$, and $\Gamma_l = \Gamma_r = 0.1$.

With the choice of initial state $|0\rangle \otimes |I, I\rangle$, one immediately finds $M^{(0)}_z = I$. The $j = 2, 3$ corrections are

$$M^{(j)}_z = \sum_m m P^{(j)}_m + \eta^j \left(g^{(j)}_I P^{(0)}_{+,I} - g^{(j)}_{I-1} P^{(0)}_{-,I} \right). \tag{B7}$$

As it turns out, in Eq. (B7) only $P^{(j)}_I$ and $P^{(j)}_{I-1}$ are different from zero, and using Eq. (B5) gives the nuclear-spin polarization:

$$\begin{aligned} M_z(t) \simeq {} & I - 2I\eta^2(1 - 2\eta(2I - 1)) \\ & \times \left(P^{(0)}_{-,I}(t) + \Gamma_l \int_0^t dt' P^{(0)}_{0,I}(t') \right), \end{aligned} \tag{B8}$$

which is plotted in Fig. 16 with and without the $O(\eta^3)$ contribution. We find that for a small η, the lowest order correction is in excellent agreement with Eq. (B1). In the inset, we show that including the third-order eliminates any visible discrepancy.

The stationary value can be obtained using $\int_0^\infty P^{(0)}_{0,I}(t)dt = (\Gamma_l + \Gamma_r)^{-1}$:

$$M_z(t \to \infty) \simeq I - 2I\eta^2(1 - 2\eta(2I - 1)) \frac{2\Gamma_l + \Gamma_r}{\Gamma_l + \Gamma_r}, \tag{B9}$$

which omitting the $O(\eta^3)$ contribution, is Eq. (43) of the main text.

[1] W. A. Coish and J. Baugh, Phys. Status Solidi B **246**, 2203 (2009).

[2] E. A. Chekhovich, M. N. Makhonin, A. I. Tartakovskii, A. Yacoby, H. Bluhm, K. C. Nowack, and L. M. K. Vandersypen, Nat. Mater. **12**, 494 (2013).

[3] W. Yang, W.-L. Ma, and R.-B. Liu, Rep. Prog. Phys. **80**, 016001 (2017).

[4] J. M. Taylor, A. Imamoglu, and M. D. Lukin, Phys. Rev. Lett. **91**, 246802 (2003).

[5] B. Hensen, W. W. Huang, C.-H. Yang, K. W. Chan, J. Yoneda, T. Tanttu, F. E. Hudson, A. Laucht, K. M. Itoh, T. D. Ladd *et al.*, Nat. Nanotechnol. **15**, 13 (2020).

[6] J. J. Pla, K. Y. Tan, J. P. Dehollain, W. H. Lim, J. J. L. Morton, F. A. Zwanenburg, D. N. Jamieson, A. S. Dzurak, and A. Morello, Nature (London) **496**, 334 (2013).

[7] T. van der Sar, Z. H. Wang, M. S. Blok, H. Bernien, T. H. Taminiau, D. M. Toyli, D. A. Lidar, D. D. Awschalom, R. Hanson, and V. V. Dobrovitski, Nature (London) **484**, 82 (2012).

[8] C. E. Bradley, J. Randall, M. H. Abobeih, R. C. Berrevoets, M. J. Degen, M. A. Bakker, M. Markham, D. J. Twitchen, and T. H. Taminiau, Phys. Rev. X **9**, 031045 (2019).

[9] M. D. Shulman, S. P. Harvey, J. M. Nichol, S. D. Bartlett, A. C. Doherty, V. Umansky, and A. Yacoby, Nat. Commun. **5**, 5156 (2014).

[10] M. R. Delbecq, T. Nakajima, P. Stano, T. Otsuka, S. Amaha, J. Yoneda, K. Takeda, G. Allison, A. Ludwig, A. D. Wieck *et al.*, Phys. Rev. Lett. **116**, 046802 (2016).

[11] F. K. Malinowski, F. Martins, L. Cywiński, M. S. Rudner, P. D. Nissen, S. Fallahi, G. C. Gardner, M. J. Manfra, C. M. Marcus, and F. Kuemmeth, Phys. Rev. Lett. **118**, 177702 (2017).

[12] F. H. L. Koppens, D. Klauser, W. A. Coish, K. C. Nowack, L. P. Kouwenhoven, D. Loss, and L. M. K. Vandersypen, Phys. Rev. Lett. **99**, 106803 (2007).

[13] S. Chesi, L.-P. Yang, and D. Loss, Phys. Rev. Lett. **116**, 066806 (2016).

[14] H. Bluhm, S. Foletti, I. Neder, M. Rudner, D. Mahalu, V. Umansky, and A. Yacoby, Nat. Phys. **7**, 109 (2011).

[15] F. K. Malinowski, F. Martins, P. D. Nissen, E. Barnes, Ł. Cywiński, M. S. Rudner, S. Fallahi, G. C. Gardner, M. J. Manfra, C. M. Marcus *et al.*, Nat. Nanotechnol. **12**, 16 (2017).

[16] J. Baugh, Y. Kitamura, K. Ono, and S. Tarucha, Phys. Rev. Lett. **99**, 096804 (2007).

[17] J. R. Petta, J. M. Taylor, A. C. Johnson, A. Yacoby, M. D. Lukin, C. M. Marcus, M. P. Hanson, and A. C. Gossard, Phys. Rev. Lett. **100**, 067601 (2008).

[18] G. Giavaras, N. Lambert, and F. Nori, Phys. Rev. B **87**, 115416 (2013).

[19] M. Eto, T. Ashiwa, and M. Murata, J. Phys. Soc. Jpn. **73**, 307 (2004).

[20] E. M. Kessler, S. Yelin, M. D. Lukin, J. I. Cirac, and G. Giedke, Phys. Rev. Lett. **104**, 143601 (2010).

[21] M. J. A. Schuetz, E. M. Kessler, J. I. Cirac, and G. Giedke, Phys. Rev. B **86**, 085322 (2012).

[22] S. Chesi and W. A. Coish, Phys. Rev. B **91**, 245306 (2015).

[23] R. H. Dicke, Phys. Rev. **93**, 99 (1954).

[24] V. Degiorgio and F. Ghielmetti, Phys. Rev. A **4**, 2415 (1971).

[25] M. Gross and S. Haroche, Phys. Rep. **93**, 301 (1982).

[26] W.-B. He, S. Chesi, H.-Q. Lin, and X.-W. Guan, Phys. Rev. B **99**, 174308 (2019).

[27] L. Y. Gorelik, A. Isacsson, M. V. Voinova, B. Kasemo, R. I. Shekhter, and M. Jonson, Phys. Rev. Lett. **80**, 4526 (1998).

[28] L. Y. Gorelik, A. Isacsson, M. Jonson, B. Kasemo, R. I. Shekhter, and M. V. Voinova, Physica B: Condens. Matter **249–251**, 197 (1998).

[29] A. Isacsson, L. Y. Gorelik, M. V. Voinova, B. Kasemo, R. I. Shekhter, and M. Jonson, Physica B: Condens. Matter **255**, 150 (1998).

[30] L. Gorelik, S. Kulinich, Y. Galperin, R. I. Shekhter, and M. Jonson, Phys. Usp. **41**, 178 (1998).

[31] L. Y. Gorelik, A. Isacsson, Y. M. Galperin, R. I. Shekhter, and M. Jonson, Nature (London) **411**, 454 (2001).

[32] H. K. Park, J. Park, A. K. L. Lim, E. H. Anderson, A. P. Alivisatos, and P. L. McEuen, Nature (London) **407**, 57 (2000).

[33] D. V. Scheible and R. H. Blick, Appl. Phys. Lett. **84**, 4632 (2004).

[34] T. Novotny, A. Donarini, C. Flindt, and A. P. Jauho, Phys. Rev. Lett. **92**, 248302 (2004).

[35] F. Pistolesi and R. Fazio, Phys. Rev. Lett. **94**, 036806 (2005).

[36] A. Donarini, T. Novotny, and A. P. Jauho, New J. Phys. **7**, 237 (2005).

[37] F. Pistolesi, Phys. Rev. B **69**, 245409 (2004).

[38] A. Romito and Y. V. Nazarov, Phys. Rev. B **70**, 212509 (2004).

[39] T. Fujita, T. A. Baart, C. Reichl, W. Wegscheider, and L. M. K. Vandersypen, npj Quantum Inf. **3**, 22 (2017).

[40] A. R. Mills, D. M. Zajac, M. J. Gullans, F. J. Schupp, T. M. Hazard, and J. R. Petta, Nat. Commun. **10**, 1063 (2019).

[41] A. Khaetskii, D. Loss, and L. Glazman, Phys. Rev. B **67**, 195329 (2003).

[42] W. A. Coish, D. Loss, E. A. Yuzbashyan, and B. L. Altshuler, J. Appl. Phys. **101**, 081715 (2007).

[43] W. Zhang, V. V. Dobrovitski, K. A. Al-Hassanieh, E. Dagotto, and B. N. Harmon, Phys. Rev. B **74**, 205313 (2006).

[44] L. Chirolli and G. Burkard, Adv. Phys. **57**, 225 (2008).

[45] L. J. Lauhon, M. S. Gudiksen, D. L. Wang, and C. M. Lieber, Nature (London) **420**, 57 (2002).

[46] O. Moutanabbir, D. Isheim, D. N. Seidman, Y. Kawamura, and K. M. Itoh, Appl. Phys. Lett. **98**, 013111 (2011).

[47] W. X. Lai and W. Yang, Phys. Rev. B **92**, 155433 (2015).

[48] P. Philippopoulos, S. Chesi, and W. A. Coish, Phys. Rev. B **101**, 115302 (2020).

[49] R. I. Shekhter, Y. Galperin, L. Y. Gorelik, A. Isacsson, and M. Jonson, J. Phys.: Condens. Matter **15**, R441 (2003).

[50] A. Angerer, K. Streltsov, T. Astner, S. Putz, H. Sumiya, S. Onoda, J. Isoya, W. J. Munro, K. Nemoto, J. Schmiedmayer *et al.*, Nat. Phys. **14**, 1168 (2018).

[51] H. Bluhm, S. Foletti, D. Mahalu, V. Umansky, and A. Yacoby, Phys. Rev. Lett. **105**, 216803 (2010).

[52] J. M. Elzerman, R. Hanson, L. H. Willems van Beveren, B. Witkamp, L. M. K. Vandersypen, and L. P. Kouwenhoven, Nature (London) **430**, 431 (2004).

[53] M. Atatüre, J. Dreiser, A. Badolato, A. Högele, K. Karrai, and A. Imamoglu, Science **312**, 551 (2006).

[54] M. Atature, J. Dreiser, A. Badolato, and A. Imamoglu, in *Optical Control of Quantum-dot Spin States* (Pan Stanford Publishing, Singapore, 2009), pp. 151–166.

[55] S. Foletti, H. Bluhm, D. Mahalu, V. Umansky, and A. Yacoby, Nat. Phys. **5**, 903 (2009).

[56] M. Gullans, J. J. Krich, J. M. Taylor, H. Bluhm, B. I. Halperin, C. M. Marcus, M. Stopa, A. Yacoby, and M. D. Lukin, Phys. Rev. Lett. **104**, 226807 (2010).

[57] E. A. Chekhovich, A. Ulhaq, E. Zallo, F. Ding, O. G. Schmidt, and M. S. Skolnick, Nat. Mater. **16**, 982 (2017).

[58] S. Tarucha and J. Baugh, J. Phys. Soc. Jpn. **77**, 031011 (2009).

[59] L. B. Gravert, P. Lorenz, C. Nase, J. Stolze, and G. S. Uhrig, Phys. Rev. B **94**, 094416 (2016).

[60] C. X. Deng and X. D. Hu, Phys. Rev. B **72**, 165333 (2005).

[61] G. Ramon and X. D. Hu, Phys. Rev. B **75**, 161301(R) (2007).

[62] R. Takahashi, K. Kono, S. Tarucha, and K. Ono, Phys. Rev. Lett. **107**, 026602 (2011).

[63] R. de Sousa and S. Das Sarma, Phys. Rev. B **68**, 115322 (2003).

[64] J. J. L. Morton, A. M. Tyryshkin, R. M. Brown, S. Shankar, B. W. Lovett, A. Ardavan, T. Schenkel, E. E. Haller, J. W. Ager, and S. A. Lyon, Nature (London) **455**, 1085 (2008).

[65] M. Steger, K. Saeedi, M. L. W. Thewalt, J. J. L. Morton, H. Riemann, N. V. Abrosimov, P. Becker, and H.-J. Pohl, Science **336**, 1280 (2012).

[66] K. Saeedi, S. Simmons, J. Z. Salvail, P. Dluhy, H. Riemann, N. V. Abrosimov, P. Becker, H.-J. Pohl, J. J. Morton, and M. L. Thewalt, Science **342**, 830 (2013).

[67] J. T. Muhonen, J. P. Dehollain, A. Laucht, F. E. Hudson, R. Kalra, T. Sekiguchi, K. M. Itoh, D. N. Jamieson, J. C. McCallum, A. S. Dzurak *et al.*, Nat. Nanotechnol. **9**, 986 (2014).

[68] A. Milton and I. A. Stegun, *Handbook of Mathematical Functions: With Formulas, Graphs, and Mathematical Tables* (Dover, New York, 1970).

[69] Y. Tokura, W. G. van der Wiel, T. Obata, and S. Tarucha, Phys. Rev. Lett. **96**, 047202 (2006).

[70] M. Pioro-Ladriere, T. Obata, Y. Tokura, Y.-S. Shin, T. Kubo, K. Yoshida, T. Taniyama, and S. Tarucha, Nat. Phys. **4**, 776 (2008).

[71] S. Chesi, Y.-D. Wang, J. Yoneda, T. Otsuka, S. Tarucha, and D. Loss, Phys. Rev. B **90**, 235311 (2014).

[72] J. R. Petta, A. C. Johnson, J. M. Taylor, E. A. Laird, A. Yacoby, M. D. Lukin, C. M. Marcus, M. P. Hanson, and A. C. Gossard, Science **309**, 2180 (2005).

[73] D. Kim, Z. Shi, C. B. Simmons, D. R. Ward, J. R. Prance, T. S. Koh, J. K. Gamble, D. E. Savage, M. G. Lagally, M. Friesen *et al.*, Nature (London) **511**, 70 (2014).

[74] G. Schmidt, D. Ferrand, L. W. Molenkamp, A. T. Filip, and B. J. van Wees, Phys. Rev. B **62**, R4790(R) (2000).

[75] R. Jasen, J. Phys. D: Appl. Phys. **36**, R289 (2003).

[76] I. Zutic, J. Fabian, and S. C. Erwin, Phys. Rev. Lett. **97**, 026602 (2006).

[77] H. Aurich, A. Baumgartner, F. Freitag, A. Eichler, J. Trbovic, and C. Schonenberger, Appl. Phys. Lett. **97**, 153116 (2010).

[78] J. Tarun, S.-Y. Huang, Y. Fukuma, H. Idzuchi, Y.-C. Otani, N. Fukata, K. Ishibashi, and S. Oda, J. Appl. Phys. **109**, 07C508 (2011).

[79] K. Molmer, Y. Castin, and J. Dalibard, J. Opt. Soc. Am. B **10**, 524 (1993).

[80] Y. Yamamoto and A. Imamoglu, *Mesoscopic Quantum Optics* (Wiley, New York, 1999).

[81] G. Tóth, Phys. Rev. A **85**, 022322 (2012).

[82] L. Pezzè, A. Smerzi, M. K. Oberthaler, R. Schmied, and P. Treutlein, Rev. Mod. Phys. **90**, 035005 (2018).

[83] R. Prevedel, G. Cronenberg, M. S. Tame, M. Paternostro, P. Walther, M. S. Kim, and A. Zeilinger, Phys. Rev. Lett. **103**, 020503 (2009).

[84] R. E. George, W. Witzel, H. Riemann, N. V. Abrosimov, N. Nötzel, M. L. W. Thewalt, and J. J. L. Morton, Phys. Rev. Lett. **105**, 067601 (2010).

[85] G. W. Morley, M. Warner, A. M. Stoneham, P. T. Greenland, J. van Tol, C. W. M. Kay, and G. Aeppli, Nat. Mater. **9**, 725 (2010).

[86] V. Mourik, S. Asaad, H. Firgau, J. J. Pla, C. Holmes, G. J. Milburn, J. C. McCallum, and A. Morello, Phys. Rev. E **98**, 042206 (2018).

[87] S. Asaad, V. Mourik, B. Joecker, M. A. I. Johnson, A. D. Baczewski, H. R. Firgau, M. T. Madzik, V. Schmitt, J. J. Pla, F. E. Hudson *et al.*, Nature (London) **579**, 205 (2020).

[88] D. P. Franke, F. M. Hrubesch, M. Künzl, H.-W. Becker, K. M. Itoh, M. Stutzmann, F. Hoehne, L. Dreher, and M. S. Brandt, Phys. Rev. Lett. **115**, 057601 (2015).

[89] J. J. Pla, A. Bienfait, G. Pica, J. Mansir, F. A. Mohiyaddin, Z. Zeng, Y. M. Niquet, A. Morello, T. Schenkel, J. J. L. Morton *et al.*, Phys. Rev. Appl. **9**, 044014 (2018).

[90] J. Mansir, P. Conti, Z. Zeng, J. J. Pla, P. Bertet, M. W. Swift, C. G. Van de Walle, M. L. W. Thewalt, B. Sklenard, Y. M. Niquet *et al.*, Phys. Rev. Lett. **120**, 167701 (2018).

[91] H.-P. Breuer and F. Petruccione, *The Theory of Open Quantum Systems* (Oxford University Press, New York, 2002).

[92] K. Blum, *Density Matrix Theory and Applications* (Springer, Heidelberg, 2012).

[93] D. J. Reilly, C. M. Marcus, M. P. Hanson, and A. C. Gossard, Appl. Phys. Lett. **91**, 162101 (2007).

[94] M. C. Cassidy, A. S. Dzurak, R. G. Clark, K. D. Petersson, I. Farrer, D. A. Ritchie, and C. G. Smith, Appl. Phys. Lett. **91**, 222104 (2007).